Wall-Modeled Large Eddy Simulation Method for Unstructured-Grid Navier-Stokes Solvers

Li Wang*, W. Kyle Anderson†, and Eric J. Nielsen‡
NASA Langley Research Center, Hampton, VA 23681

Prahladh S. Iyer§ and Boris Diskin¶
National Institute of Aerospace, Hampton, VA 23666

This paper reports on the implementation and assessment of a Wall-Modeled Large-Eddy Simulation (WMLES) methodology in an unstructured-grid, node-centered flow solver, FUN3D that is developed and supported at the NASA Langley Research Center. Finite-volume (FV) and finite-element (FE) discretization schemes considered in the study provide formal second-order spatial accuracy. Large-Eddy Simulations (LES) resolve large-scale turbulent-flow features and filter out small-scale effects using the Vreman subgrid-scale model. At solid-wall boundaries, a shear-stress model is employed to provide a proper boundary-flux closure. The nonlinear equations are integrated in time using either an optimized backward difference formula or an implicit multistage Runge-Kutta temporal scheme. The implicit equations at each time step are solved by strong nonlinear iteration schemes. WMLES demonstrations are shown for two high-lift configurations, namely, the McDonnell Douglas 30P30N multielement airfoil and a NASA High-Lift Common Research Model. Results show that the WMLES approaches implemented in the FV and FE discretization methods produce consistent solutions and are capable of capturing key aerodynamic characteristics and flow structures for high-lift configurations at a wide range of angles of attack including maximum-lift conditions. In the 30P30N example, correct trends in the variations of integrated aerodynamic forces and moments, surface pressure distributions, and boundary-layer profiles are captured as the Reynolds number is increased.

I. Introduction

Accurately predicting maximum lift using a computational methodology is a vital capability for achieving the goal of principally utilizing analysis methods for certifying commercial aircraft, with only minimal reliance on flight testing [1]. To assess and improve current computational fluid dynamics (CFD) technology for successfully simulating flows at maximum lift conditions, a series of workshops has been sponsored by the American Institute of Aeronautics and Astronautics (AIAA) beginning in 2010 [2–5]. For the 4th High-Lift Prediction Workshop (HLPW), recently held at the 2022 AIAA SciTech conference [5], participants presented results obtained using Reynolds-averaged Navier Stokes (RANS), Wall-Modeled Large Eddy Simulations (WMLES), and Hybrid RANS/LES (HRLES) methods. Among the methodologies presented at the workshop, the HRLES and WMLES approaches demonstrated better agreement with experimental data near maximum lift when compared to the RANS methodologies, which consistently exhibited large separated regions toward the wingtips at high angles of attack that are not present in the experiment.

For WMLES simulations, seven of the nine participating research groups presented results that successfully predicted maximum lift within two percent of experimental data. Although a nascent capability at the time, the FUN3D unstructured-grid finite-volume solver [6] was among the groups meeting this criteria. Since the workshop, the capabilities in FUN3D are continuing to evolve as additional developments are made and valuable experience is gained through subsequent applications. As part of the continuing development process, the current work has three primary objectives. First, while initial results were good, no "best practices" had been established prior to the workshop for determining grid density requirements. In fact, only three meshes had been considered for computations at the time, and extensive computations on one of the meshes were not pursued because the spacing normal to the wall was determined

*Research Aerospace Engineer, Computational AeroSciences Branch, MS 128, AIAA Associate Fellow
†Senior Research Scientist, Computational AeroSciences Branch, MS 128, AIAA Associate Fellow
‡Research Scientist, Computational AeroSciences Branch, MS 128, AIAA Associate Fellow
§Senior Research Scientist, AIAA Senior Member.
¶Senior Research Fellow, AIAA Associate Fellow.

to be excessive. Of the remaining two meshes, the finest mesh was comprised of a mixture of hexahedral and tetrahedral elements, with primarily hexahedral elements in the vicinity of the solid surfaces. While the results compared well with experimental data, as well as with other participants, the lift at one angle of attack was approximately 3% lower than the experimental value. Therefore, the first objective of this work is to examine the effects of strategic mesh refinement.

The second purpose of the current work is to provide a preliminary assessment of the finite-element capability [7] within FUN3D, which compliments the finite-volume technology that has been the primary discretization for many years. Specifically, Ref. [7] demonstrates that for RANS computations, the finite-element scheme offers accuracy advantages over the finite-volume scheme, particularly on tetrahedral meshes. Therefore, another objective of this work is to assess whether the finite-element discretization is demonstratively more accurate for WMLES applications as it is for RANS.

Finally, an important step in developing CFD for certification by analysis is the assessment of the ability to accurately simulate high-lift conditions at full-scale flight Reynolds numbers, and to compute subtle differences in flowfields associated with changes in Reynolds number. To this end, a data set consisting of force, pressure, and velocity profiles exists for nominally two-dimensional high-lift configurations at different Reynolds numbers that is well documented and readily available [8–10]. While these data have been previously used by CFD researchers for evaluating RANS methodologies [10, 11], they have been largely untapped for evaluating WMLES technology. Therefore, the last objective of the current work is to provide a preliminary assessment of the ability to compute flowfield variations, attributable to changes in Reynolds number, at two different angles of attack. For this study, pressure distributions, forces, and velocity profiles are compared with experimental data as well as with recent RANS computations.

The rest of the material in the paper is presented in the following order. Section II describes the governing equations. Section III outlines the discretization schemes including finite-volume and finite-element methods as well as the iterative solvers available in FUN3D for WMLES computations. Numerical results for flows over the McDonnell Douglas 30P30N multielement airfoil and the NASA CRM-HL configuration are presented and discussed in Section IV, where comparisons of the WMLES solutions are made with available experimental data. Finally, Section V offers conclusions and directions of future work.

II. Governing Equations

The governing equations are the compressible, spatially-filtered Navier-Stokes equations, which can be expressed in the following conservative form:

$$\frac{\partial \mathbf{Q}(\mathbf{x},t)}{\partial t} + \nabla \cdot (\mathbf{F}_e(\mathbf{Q}) - \mathbf{F}_v(\mathbf{Q}, \nabla \mathbf{Q})) = 0 \quad \text{in } \Omega \tag{1}$$

where Ω is a bounded domain. The vector of conservative flow variables, $\mathbf{Q}$, and the inviscid and viscous Cartesian flux vectors, $\mathbf{F}_e$ and $\mathbf{F}_v$, are defined as follows,

$$\mathbf{Q} = \begin{bmatrix} \rho \\ \rho u \\ \rho v \\ \rho w \\ \rho E \end{bmatrix}, \quad \mathbf{F}_e^x = \begin{bmatrix} \rho u \\ \rho u^2 + p \\ \rho uv \\ \rho uw \\ (\rho E + p)u \end{bmatrix}, \quad \mathbf{F}_e^y = \begin{bmatrix} \rho v \\ \rho uv \\ \rho v^2 + p \\ \rho vw \\ (\rho E + p)v \end{bmatrix}, \quad \mathbf{F}_e^z = \begin{bmatrix} \rho w \\ \rho uw \\ \rho vw \\ \rho w^2 + p \\ (\rho E + p)w \end{bmatrix}, \tag{2}$$

$$\mathbf{F}_v^x = \begin{bmatrix} 0 \\ \tau_{xx} \\ \tau_{xy} \\ \tau_{xz} \\ u\tau_{xx} + v\tau_{xy} + w\tau_{xz} + \kappa \frac{\partial T}{\partial x} \end{bmatrix}, \mathbf{F}_v^y = \begin{bmatrix} 0 \\ \tau_{xy} \\ \tau_{yy} \\ \tau_{yz} \\ u\tau_{xy} + v\tau_{yy} + w\tau_{yz} + \kappa \frac{\partial T}{\partial y} \end{bmatrix}, \mathbf{F}_v^z = \begin{bmatrix} 0 \\ \tau_{xz} \\ \tau_{yz} \\ \tau_{zz} \\ u\tau_{xz} + v\tau_{yz} + w\tau_{zz} + \kappa \frac{\partial T}{\partial z} \end{bmatrix}. \tag{3}$$

Here, ρ, p, and E denote the fluid density, pressure, and specific total energy per unit mass, respectively, and $\mathbf{u} = (u, v, w)$ represents components of the Cartesian velocity vector. The pressure p is determined by the equation of state for an ideal gas,

$$p = (\gamma - 1)\left(\rho E - \frac{1}{2}\rho(u^2 + v^2 + w^2)\right), \tag{4}$$

where γ is the ratio of specific heats, and $\gamma = 1.4$ for air. Note that all flow quantities represent filtered (or resolved) variables. The τ subscripts represent the components of the total (viscous and turbulent) stress tensor, which for a Newtonian fluid are defined as,

$$\tau_{ij} = (\mu + \mu_T)\left(\frac{\partial \mathbf{u}_i}{\partial \mathbf{x}_j} + \frac{\partial \mathbf{u}_j}{\partial \mathbf{x}_i} - \frac{2}{3}\frac{\partial \mathbf{u}_k}{\partial \mathbf{x}_k}\delta_{ij}\right). \tag{5}$$

Here, δ_{ij} is the Kronecker delta operator and subscripts i, j, k refer to the Cartesian coordinates $\mathbf{x} = (x, y, z)$. The notations κ and T denote the total thermal conductivity and temperature, respectively, and satisfy the following relation:

$$\kappa T = \gamma\left(\frac{\mu}{Pr} + \frac{\mu_T}{Pr_T}\right)\left(E - \frac{1}{2}\left(u^2 + v^2 + w^2\right)\right). \tag{6}$$

In Eqs. (5) and (6), μ refers to the dynamic viscosity, which is obtained via Sutherland's law[12], and μ_T denotes the modeled subgrid-scale (SGS) viscosity; Pr and Pr_T are the mean-flow Prandtl number and the turbulent Prandtl number that are set to be 0.72 and 0.9, respectively. In the present work, μ_T is obtained using the model presented in Ref. [13], which is summarized below:

$$\mu_T = \rho C\sqrt{\frac{B_\beta}{\alpha_{ij}\alpha_{ij}}}, \tag{7}$$

where

$$\alpha_{ij} = \frac{\partial u_j}{\partial x_i}, \tag{8}$$

$$\beta_{ij} = \Delta_m^2 \alpha_{mi}\alpha_{mj}, \tag{9}$$

$$B_\beta = \beta_{11}\beta_{22} - \beta_{12}^2 + \beta_{11}\beta_{33} - \beta_{13}^2 + \beta_{22}\beta_{33} - \beta_{23}^2. \tag{10}$$

The modeling constant, C, is related to the Smagorinsky constant as follows, $C \approx 2.5C_s^2$ and $C_s = 0.17$, as suggested in Ref. [13]. The local filter width, Δ_m ($m = 1, 2,$ and 3), is currently set to be the cube root of the cell volume in both FV and FE discretizations, based on the use of nearly isotropic grids. All the WMLES computations conducted in the current work are based on use of the standard Vreman modeling coefficient. However, as discussed later in the text, future research on adjusting this parameter to account for differing element types and grid anisotropy is planned.

III. Solution Algorithm

FUN3D [14, 15] solves the governing equations discretized on unstructured, mixed-element grids comprised of tetrahedra, pyramids, prisms, and hexahedra. Both finite-volume and finite-element discretization methods have been considered in this work, and an overview of each method is discussed below.

1. Finite-Volume Discretization

In the finite-volume discretization, median-dual control volumes are constructed around grid points. Inviscid fluxes are computed at edge medians by using an approximate Riemann solver. In the current study, Roe's flux-difference splitting [16] is used. For second-order accuracy, density, pressure, and velocity at edge medians are reconstructed by an unstructured monotonic upstream scheme for conservation laws (UMUSCL) [17, 18]. For mixed-element grids, the UMUSCL parameter, which controls the amount of dissipation in the scheme, is initialized as $\kappa_u = 0.5$. To reduce dissipation in later stages of the solution process, this parameter is increased to $\kappa_u = 0.9$ for edges where both end points are interior points, while $\kappa_u = 0.5$ is maintained for edges with at least one end point attaching to a solid surface. Note that as the κ_u parameter approaches unity, the scheme tends toward central differencing. For discretization of the viscous fluxes, the Green-Gauss theorem is used to compute cell-based gradients. In the case of tetrahedral grids, this approach is equivalent to a Galerkin-type approximation. For nontetrahedral grids, cell-based Green-Gauss gradients are combined with edge-based gradients to improve stability of viscous operators and prevent odd-even decoupling. Specifically, an edge-normal augmentation scheme [19] is used. The viscous fluxes are second-order accurate on general mixed-element grids [20, 21] including transition regions with different element types.

The boundary conditions used in the present study include a farfield Riemann solver, symmetry plane, periodic plane, and viscous-wall boundary conditions. At the farfield, the boundary conditions are weakly enforced by constructing an

exterior state based on the freestream conditions to close the boundary fluxes. The symmetry boundary conditions strongly enforce zero normal velocity at the boundary grid points, while the tangential momentum, mass, and energy conservation at the symmetry plane are enforced weakly through the conservation equations. The periodic boundary conditions combine the residuals and Jacobian matrices for pairs of nodes preidentified on the periodic planes, resulting in identical solutions for the node pairs.

The WMLES implementation largely follows the methodology described in Ref. [22]. At each time step, flowfield variables are extracted at predetermined exchange locations, which correspond to the first point off the wall in the present work. The extracted solutions serve as input to a simple equilibrium wall model [23] to determine the local shear stress at each grid point on the solid-wall surface. Once the shear stress is determined, it is used to compute boundary-face fluxes required for evaluating the residuals at the boundary grid points. An implementation of wall functions for RANS simulations has been previously reported in Ref. [24]. The implementation in the current work based on the FV discretizations is similar, albeit with some modifications; most notably, the nonlinear equation [23] that is solved to compute the wall shear stress is fully linearized in the current implementation. Proper linearizations of the wall-model boundary fluxes have been implemented to solve the system of equations implicitly.

The solution at each time step is obtained using an optimized second-order accurate implicit time-stepping scheme [25]. At each time step, the discrete nonlinear system of equations can be expressed as:

$$\mathbf{R}(\mathbf{Q}) = \mathbf{0}, \tag{11}$$

where $\mathbf{Q}$ denotes the flow solution and $\mathbf{R}$ denotes the nonlinear unsteady residual. This nonlinear system of equations at each time step is solved by an approximate Newton-type method with a pseudotime term expressed as:

$$\left[\frac{V}{\Delta\tau}\mathbf{I} + \widetilde{\frac{\partial \mathbf{R}}{\partial \mathbf{Q}}} \right] \Delta\mathbf{Q} = -\mathbf{R}(\mathbf{Q}^n), \tag{12}$$

$$\mathbf{Q}^{n+1} = \mathbf{Q}^n + \omega\, \Delta\mathbf{Q}. \tag{13}$$

Here, V is a dual-cell volume; $\Delta\tau$ is the local pseudotime step governed by the Courant-Friedrichs-Lewy (CFL) number; $\mathbf{I}$ is the identity matrix; the superscript n is the nonlinear iteration index, and ω is an underrelaxation parameter. Note that because $\mathbf{R}(\mathbf{Q})$ represents the unsteady residual, the physical time derivative is included in Eq. (11), although it is not explicitly shown. The approximate linearization, $[\widetilde{\partial \mathbf{R}/\partial \mathbf{Q}}]$ in Eq. (12), also includes the contributions from the time derivatives.

Two nonlinear solution methods are available in FUN3D: a simple defect-correction solver and a strong nonlinear iteration solver. The defect-correction method solves the linear system shown in Eq. (12) with multicolor point-implicit Gauss-Seidel (GS) iterations together with linear CFL ramping. The strong nonlinear solver, referred to as a hierarchical adaptive nonlinear iteration method (HANIM), uses additional hierarchies including a matrix-free Newton-Krylov scheme for the linear system and an adaptive CFL strategy to improve robustness and efficiency. More details of the solution methods can be found in Ref. [26]. Specification of solver parameters is given in Section IV for each test case.

2. Finite-Element Discretization

The finite-element method in FUN3D is a Petrov-Galerkin discretization previously described in Refs. [7] and [27]. For the current study, spatial accuracy is limited to nominally linear (P1) elements and the temporal discretization utilizes a second-order accurate two-stage implicit Runge-Kutta scheme described in Ref. [28]. The solution is obtained at each time step using a subiterative procedure, where the time-dependent residual is fully linearized, including all boundary conditions as well as the wall function [23], which is used at each Gauss point of every surface element to determine the local wall shear stress. For each time step, a CFL controller is used to achieve global convergence and the linear system is solved using a preconditioned generalized minimal residual (GMRES) method [29, 30] as implemented using the sparse linear algebra toolkit described in Ref. [31]. At every subiteration, the linear residual is reduced by five orders of magnitude, and the nonlinear residual is also typically reduced at least five orders of magnitude. Similar to the approach used in the finite-volume scheme, the dissipation is globally reduced once the forces start to asymptote to a final value. This reduction in dissipation is easily achieved because the scheme can be considered as a central-difference scheme with added dissipation, which can be explicitly reduced. Finally, while the boundary conditions are generally very similar to those implemented in the finite-volume scheme, the finite-element branch does not currently include periodic boundary conditions, which are being developed.

IV. Numerical Results

In this section, WMLES solutions are assessed for flows over high-lift configurations, including the McDonnell Douglas 30P30N multielement airfoil and the NASA CRM-HL aircraft model. In the 30P30N multielement airfoil example, the purpose of the computations is to evaluate the WMLES capabilities to discern differences in key aerodynamic characteristics and boundary-layer profiles for two Reynolds numbers at different angles of attack. In the high-lift CRM example, the emphasis centers on assessment of WMLES simulations for predicting maximum-lift ($C_{L,max}$) in support of the certification by analysis endeavor. For the CRM-HL cases, simulation results from both the node-centered finite-volume and stabilized finite-element methods in FUN3D are included and compared with experimental data.

A. McDonnell Douglas 30P30N Multielement Airfoil

The first high-lift configuration investigated in this paper is the McDonnell Douglas three-element airfoil [8, 9], which was tested in the NASA Langley Low Turbulence Pressure Tunnel (LTPT) [32]. The high-lift configuration is derived from a reference 11.55% thick supercritical airfoil with a chord in the stowed position of 22 inches. In the high-lift geometry, the slat chord is 14.48% and the flap chord is 30% of the reference airfoil chord. The airfoil was configured in a typical landing configuration with slat and flap deflections both set to 30° [33] .

This same configuration has previously been used for assessing RANS and LES models for computing high-lift flows [33–36]. In the present work, the freestream Mach number is 0.2 for all cases and two Reynolds numbers are considered, with two angles of attack simulated at each Reynolds number. Specifically, the Reynolds numbers, based on the chord of the airfoil in the undeflected position, are 5 million and 9 million, and nominal angles of attack of $\alpha = 8°$ and $\alpha = 16°$ are simulated at each Reynolds number. Note that for the nominally 8° case, slight differences in the angles of attack are used for each Reynolds number; these differences are denoted on the accompanying figures.

The LTPT experimental data used to compare with WMLES results includes force and moment data, pressure distributions, and mean velocity profiles. As mentioned previously, the focus of the present investigation is to assess how accurately WMLES can successfully capture key aerodynamic characteristics and boundary-layer profiles for high-lift flows as the Reynolds number is varied. Note that for this study, the two angles of attack are not in the immediate range of angles of attack where maximum lift occurs in the experiment. As described in Ref. [9], pressure data taken along the span at several chordwise stations on the airfoil clearly indicate that at $\alpha = 21°$, which yields the maximum lift, the data can no longer be considered to be two dimensional. As such, attempting to compare nominally two-dimensional simulations with three-dimensional experiments adds little value.

For the results presented, RANS solutions are also shown that have been computed using the finite-element branch of FUN3D, where the negative Spalart-Allmaras one-equation (SA-neg) model [37] is used as the turbulence model. These results are included to serve as numerical references. As mentioned previously, the finite-element solver has not been used for WMLES simulations of this configuration because periodic boundary conditions are not currently implemented.

1. Computational Grids and Solver Settings

For the WMLES computations, the configuration is extruded in the spanwise direction with the extent of $0.04c$, where c is the chord length of the airfoil in the undeflected position. This extent is fairly small and may hinder the resolution of some three-dimensional effects between the side-wall planes. In addition to the three-dimensional nature of the experimental data at high angles of attack, this relatively small spanwise extent is another reason that computations are not considered for simulation near maximum lift. The computational domain extends to $100c$ where farfield boundary conditions are imposed. Periodic boundary conditions are applied on the side planes, at $y = 0$ and $y = 0.04c$, and a total of 44 equally-spaced parallel computational planes are used in the spanwise direction so that the spacing between the planes is slightly larger than $0.0009c$. The streamwise surface spacing over the majority of the airfoil is also approximately $0.0009c$, although in the immediate vicinity of the leading and trailing edges, the spacing is finer by a factor of 5. The average of the wall-normal spacing is $0.00032c$, which corresponds to a nominal $\Delta y_w^+ \approx 100$ based on a flat-plate approximation at the freestream conditions and reference length c. The wall-normal spacing grows with a rate of 1.05 for 25 grid layers away from the wall. This computational grid contains 17.2 million points with 16.5 million hexahedra and 400,000 prisms.

Several views of the WMLES grid are provided in Figs. 1(a)–1(c). Closeup views are shown near the slat trailing edge in Fig. 1(b), and the flap leading edge and its upper surface areas in Fig. 1(c). A qualitatively similar grid has also

been generated for RANS simulations at the same test conditions, which has highly stretched elements in the boundary layer and a fine wall-normal spacing of $\Delta y_w^+ \approx 0.3$ based on the flat-plate approximation. The grid used for RANS simulations consists of a total of two planes in the spanwise direction for 2D simulations; each plane has 606,030 grid points and the spanwise extruded cells are comprised with 598,100 hexahedra and 11,086 prisms. The RANS grid is shown in Figs. 1(d)–1(f); clustered points can be seen near the airfoil surface to provide the boundary layer the resolution necessary for RANS calculations. As seen in the figures, the point distributions outside of the boundary layer are almost identical between the WMLES and RANS grids.

Views of the surface and periodic side-wall mesh for the WMLES grid are shown in Fig. 2. Here, Fig. 2(a) shows the surface mesh of the slat, whereas Fig. 2(b) shows the surface mesh near the trailing edge of the main element and the

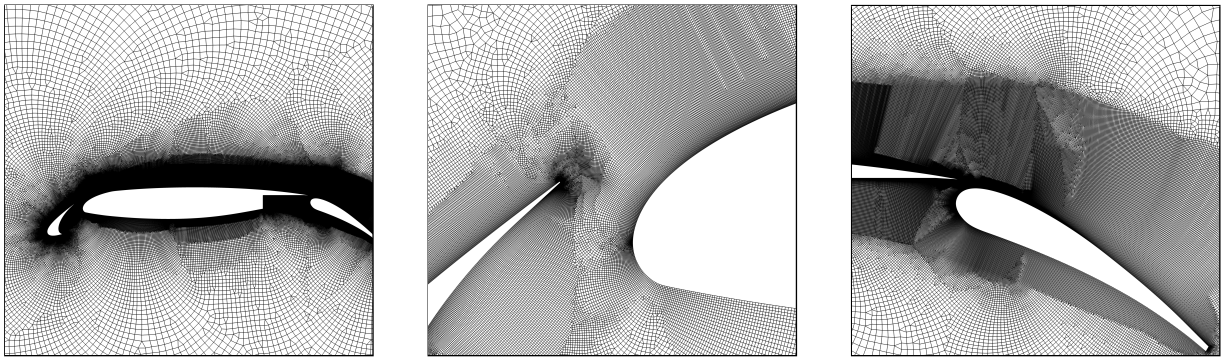

(a) Overview, WMLES (b) Slat trailing edge areas, WMLES (c) Flap, WMLES

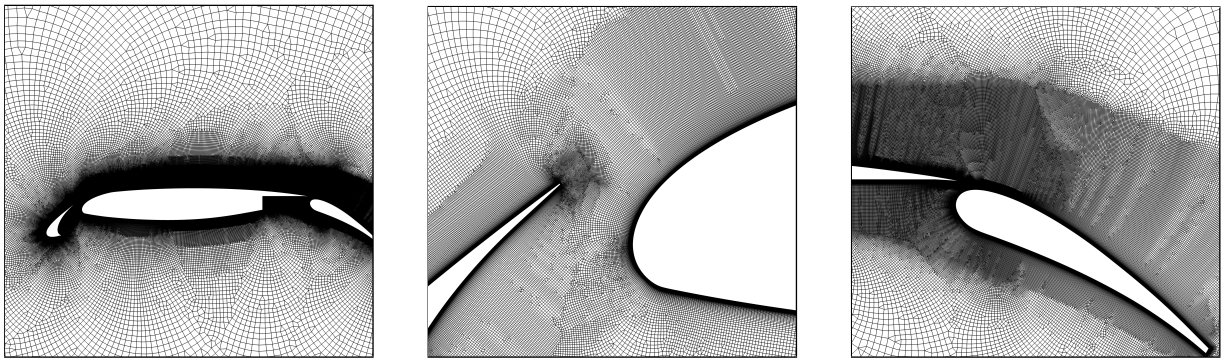

(d) Overview, RANS (e) Slat trailing edge areas, RANS (f) Flap, RANS

Fig. 1 Computational grids used for WMLES and RANS computations of 30P30N airfoil.

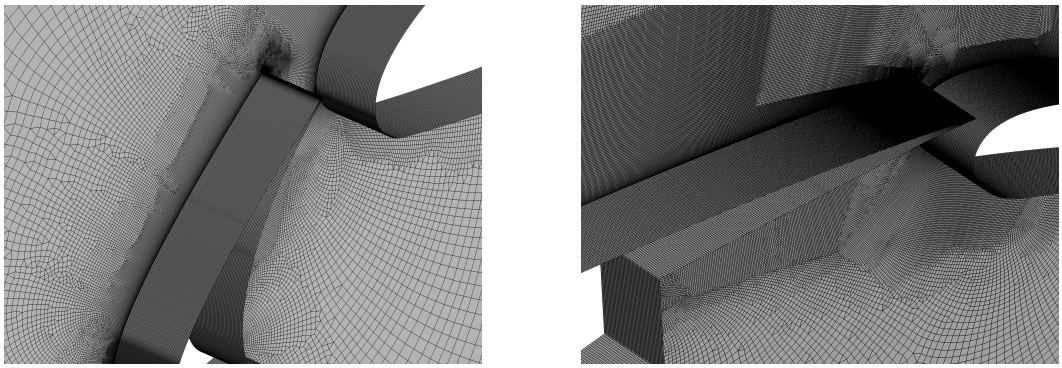

(a) Surface mesh near slat and main element (b) Surface mesh near main element and flap

Fig. 2 Surface mesh for 30P30N airfoil used for WMLES computations.

leading edge of the flap. With the exception of the leading and trailing edge areas, the ratio of streamwise to spanwise spacing of the surface elements is close to unity over the majority of the surface.

To identify approximately how many grid points are present in the log layer at several chordwise locations, Fig. 3 depicts point distributions of the WMLES grid in the boundary-layer of the 30P30N airfoil in terms of the logarithmic law of the wall. Multiple stations referenced to the airfoil in the undeflected position are considered, including one station near the slat trailing edge, three stations on the main element, and two stations on the flap. In the plot for each station, the black line represents the dimensionless velocity (u^+) as a function of the dimensionless wall coordinate (y^+), obtained by a finite-element RANS simulation for the case of Re = 9M (million) and $\alpha = 16°$; the (isolated) black dots represent locations of the present WMLES mesh points within the profile obtained by interpolating these near-wall grid points onto the u^+-y^+ plot; the red line represents the law of the wall. Several observations can be made based on analyzing these profiles. First, the black dots at the smallest y^+ value in each plot indicates the actual wall-normal spacing on the WMLES grid at the corresponding station. Except for the station of $x/c = 0.85$, most of the stations analyzed here show a wall-normal spacing close to $\Delta y_w^+ \approx 50$–100. At station $x/c = 0.85$, this value is reduced to be around $\Delta y_w^+ \approx 10$. Secondly, at most stations, only a few grid points on the WMLES mesh are actually contained within the log layer, with the exception being at $x/c = 0.85$, which contains as many as 20 points in the log layer.

To estimate the number of points in the boundary layer, consider a representative chordwise station of $x/c = 0.45$ in Fig. 3. Simply counting the number of mesh points through the log and wake layers, the boundary-layer at this location is estimated to contain roughly 17–20 points. Estimates of the thickness in terms of percentage of chord can be surmised

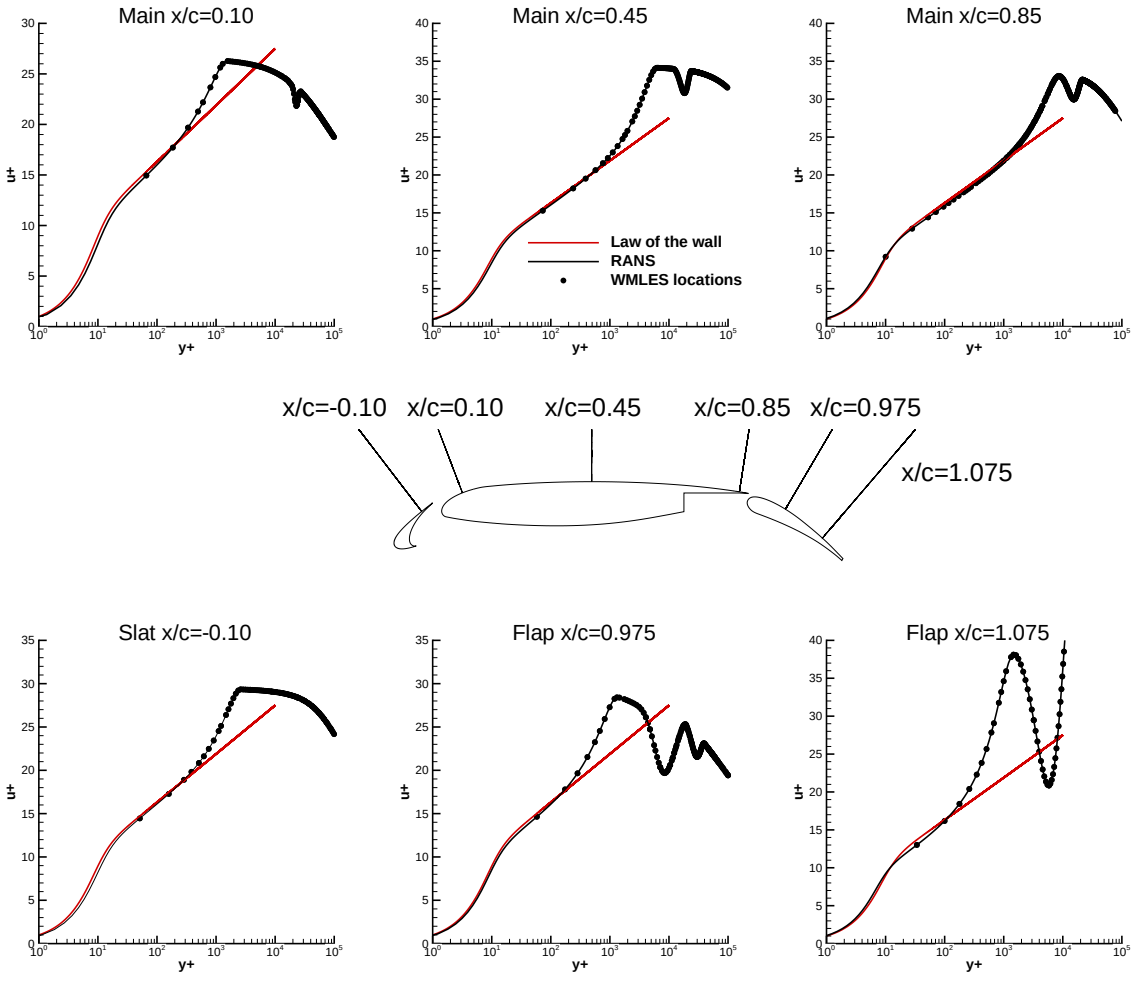

Fig. 3 Point distributions for WMLES grid in a log-layer profile at various stations (Re = 9M, $\alpha = 16°$).

using profiles from computations that are shown in the next section, where the thickness of the boundary-layer at this location is estimated to be approximately $0.009c$ for $\alpha = 8.10^\circ$ and $0.01c$ for $\alpha = 16.21^\circ$ at $Re = 9$M.

In this example, the FUN3D-FV solver is employed for all WMLES computations with the second-order backward difference formula BDF2opt [25] for the time integration. The set of time-dependent meanflow equations is solved using the legacy defect-correction solver together with 20 subiterations and 15 linear GS sweeps per subiteration. Using this strategy, the residuals are reduced by over 3 orders of magnitude at each time step. The WMLES simulations are initially conducted with a time step so that 1,000 time steps represent a single convective time unit (CTU), which is defined as the time required for flow to traverse through one characteristic length based on the freestream velocity, i.e., CTU $\equiv c/U_\infty$. After the transients are eliminated, the time step size is reduced to 2,000 time steps per CTU. Time-averaged solution quantities such as velocities, density, and pressure are collected for 10 flow passes after the statistics are converged. Integrated aerodynamic quantities are then obtained based on time-averaged quantities for WMLES. The Vreman SGS model described in Section II is employed for the WMLES calculations, using the standard model coefficient. All RANS solutions are obtained using FUN3D-FE with the negative SA-neg turbulence model where the residuals of the mean flow and turbulence-model equations are reduced to machine precision in all test cases.

2. Assessments of WMLES solutions

The computed forces and moments for the test cases considered in this example are summarized in Table 1, including the WMLES and RANS solutions as compared to the experimental data. Increments in the integrated lift, drag, and pitching moment at each angle of attack due to the increase in the Reynolds number can be derived. Both the WMLES and RANS solutions show the correct trends in the force and moment variations compared to the experiment. For example, as the Reynolds number increases from 5M to 9M, the lift increases due to reduced flap separation [33]; this is reflected in both experimental and numerical results. At $\alpha = 8^\circ$, the predicted lift increase obtained from WMLES is within 6.9% of the experimental measurement, and is improved at $\alpha = 16^\circ$ with a reduced variation of 3.0% compared to the experiment. The incremental differences obtained from RANS exhibit somewhat larger errors when compared to experiment, so that at $\alpha = 8^\circ$ the lift increments are approximately 30% different than experiment and at $\alpha = 16^\circ$ the differences are about 50%.

The drag decrease attributable to a reduction of flap separation is also captured by both WMLES and RANS for both angles of attack. However, the computed drag decrease is somewhat higher than the experiment so that at $\alpha = 8^\circ$ WMLES overpredicts the drag decrease by 22% whereas RANS overpredicts this same increment by almost 220%. At $\alpha = 16^\circ$, both WMLES and RANS again overpredict the drag decrease caused by increasing the Reynolds number by about 70% and 50%, respectively. Note that the lift may be a better metric for comparison than drag or pitching moment because the experimental configuration includes slat and flap brackets, as well as sidewall ventilation, none of which are accounted for in the computations.

Table 1 30P30N force and moment coefficients.

Re	α (°)	c_l			c_d			c_m		
		Experiment	WMLES	RANS	Experiment	WMLES	RANS	Experiment	WMLES	RANS
5×10^6	8.12	3.0841	3.2872	3.2994	0.0361	0.0396	0.0405	-0.5701	-0.6134	-0.6140
9×10^6	8.10	3.1354	3.3352	3.3386	0.0278	0.0328	0.0379	-0.5872	-0.6236	-0.6234
5×10^6	16.21	3.8932	4.1377	4.1234	0.0379	0.0626	0.0562	-0.4591	-0.4993	-0.4904
9×10^6	16.21	3.9763	4.2184	4.1787	0.0359	0.0557	0.0524	-0.4707	-0.5121	-0.5002

Computed surface pressure distributions from WMLES and RANS computations at different Reynolds numbers are shown in Figs. 4 and 5 for $\alpha = 8^\circ$ and $\alpha = 16^\circ$, respectively. Experimental data are included for the Reynolds numbers and angles of attack considered here. The pressures on the slat, main element, and flap are plotted separately for better comparisons; the separate pressure comparisons are laid out from left to right in these plots for each data set. At the lower angle of attack of 8°, the WMLES solutions show higher upper-surface suction than the experiment. However, a consistent solution is shown in the RANS results in Fig 4(b) and in Ref. [33]. The pressures on the main element are slightly overpredicted in the WMLES solutions, indicating slightly more circulation than was present in the experiment, which also contributes to the larger lift on the slat. Similarly, the WMLES solutions obtain a slightly higher suction level on the upper surface of the flap than that shown in the experiment, but the difference is fairly small. On the pressure side of each element, the solutions are seen to be accurate for the WMLES solutions, including in the

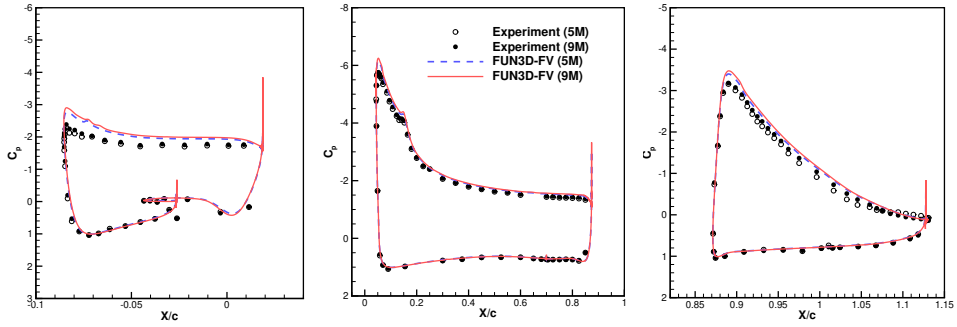

(a) WMLES

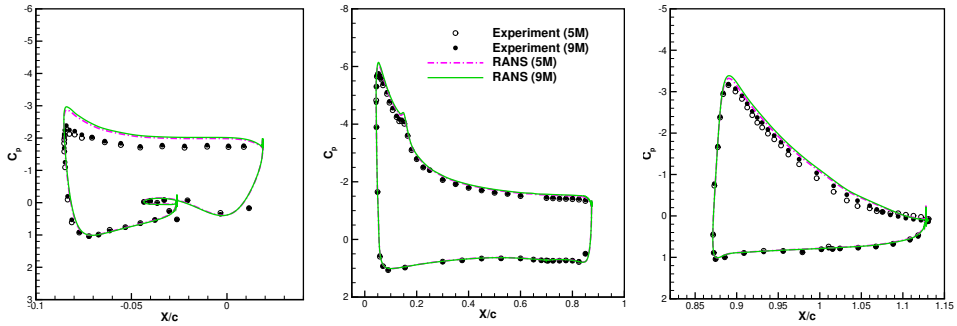

(b) RANS

Fig. 4 Comparison of pressure distributions on 30P30N at 8 degrees.

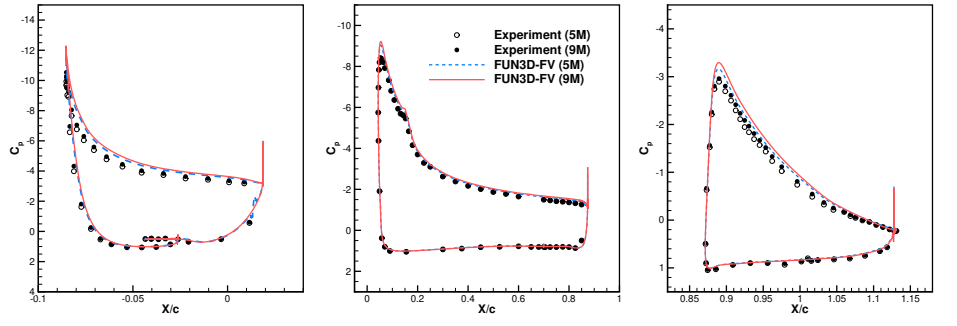

(a) WMLES

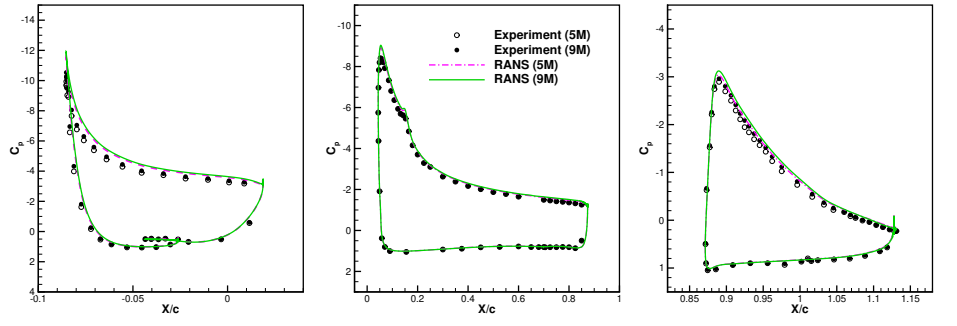

(b) RANS

Fig. 5 Comparison of pressure distributions on 30P30N at 16 degrees.

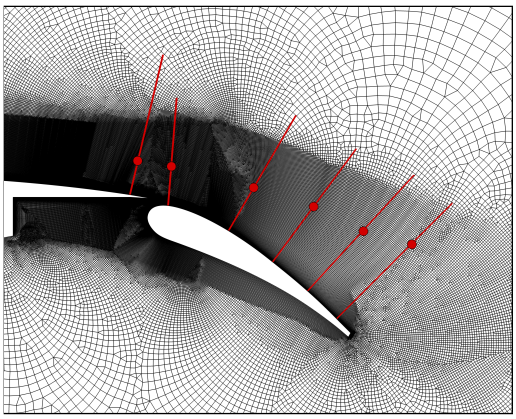

Fig. 6 Overview of mesh resolution for WMLES at velocity-profile locations (left to right: $x/c = 0.85, 0.8982, 0.975, 1.032, 1.075,$ **and** 1.1125**).**

vicinity of the stagnation points of the flow (corresponding to $C_p = 1.0$). It should be noted that, compared to the experimental data, the trends in surface pressure variations with increasing Reynolds number are also well captured, and moreover, WMLES and RANS results are both in good agreement. For the cases of $\alpha = 16^\circ$, consistent solutions are again observed between the WMLES and RANS results, including similar suction peaks on the slat and the main element. Compared to the experiments, the agreement of slat suction pressure is improved at the higher angle of attack. The trends in the surface pressure variations due to the increase of the Reynolds number are again well captured.

Next, the computed velocity profiles at specified stations are provided and compared with experimental data. To examine the suitability of the current mesh for capturing the wakes over the flap, an overview of the WMLES grid is illustrated in Fig. 6 that includes the experimental locations for the centerline of the wake at $\alpha = 16^\circ$. In this figure, it can be seen that mesh density decreases as the trailing edge of the flap is approached. Figures 7 and 8 depict velocity profiles for four stations, including one station ($x/c = 0.45$) on the main element and three stations ($x/c = 0.8982, 1.032,$ and 1.1125) on the flap, for the cases of $\alpha = 8^\circ$ and $\alpha = 16^\circ$, respectively. The positions of these stations are relative to the airfoil in the undeflected position and can be determined by cross-referencing the profile locations shown in Figs. 3 and 6. Overall good agreement is observed between the WMLES computations and the experimental data at both angles of attack, and variations of the velocity profiles due to increasing the Reynolds number are well predicted. However, at station $x/c = 1.1125$ at $\alpha = 16^\circ$, there is a crossing of the profiles in the experimental data at a distance of about 0.1 that is not captured in the simulation. At the midchord of the main element ($x/c = 0.45$), the WMLES solution also shows a slightly thicker boundary layer, which may be caused by insufficient mesh resolution in the boundary layer upstream of this location (c.f., $x/c = 0.10$ in Fig. 3), or some differences in the laminar-turbulent transition locations between the simulations and experiments. A further investigation will be needed to get better understanding of the cause. Overall though, the boundary layer thickness, as well as the magnitudes and shapes of various wakes are captured accurately at most of the stations.

Velocity profiles obtained from RANS simulations are shown in Figs. 7(e)–7(h) and 8(e)–8(h). Here, it is seen that the wake deficits seem to be somewhat deeper and more accurately captured than in the WMLES simulations. Also, at station $x/c = 1.1125$ at $\alpha = 16^\circ$, the crossover in the profile at a distance of approximately 0.1 is correctly represented. An interesting feature about the profiles is that at $\alpha = 8^\circ$ no slat wake is present in the experimental data. The WMLES simulations successfully captures this feature, whereas the RANS solutions clearly indicate the presence of the slat wake. In previous RANS results, reported in Ref. [10], this behavior is seen to be quite typical.

Figure 9 shows contours of instantaneous density-gradient magnitude around 30P30N at $\alpha = 8^\circ$ and $\alpha = 16^\circ$ for $Re = 5$M and 9M, obtained by the FUN3D-FV WMLES approach. Unsteadiness of the wake emanating from the slat is captured and clearly observed in the simulations. The slat wake becomes more clearly defined as either the angle of attack or the Reynolds number increases. Interestingly, even though slat wakes are visible in the instantaneous density-gradient magnitude contours at $\alpha = 8^\circ$ (Figs. 9(a) and 9(b)), this feature is averaged out in the time-varying flow fields so that there is no evidence of the slat wake in the mean-velocity profiles, as discussed previously (Figs. 7(a)–7(d)). Moreover, as the angle of attack increases, the width of various wake regions above the flap becomes more pronounced. On the other hand, as the Reynolds number is increased for a fixed angle of attack, the wakes from the slat and main element are narrower because each individual element contains thinner boundary layers. The corresponding RANS

steady-state solutions are illustrated in Fig. 10 for comparison. At $\alpha = 8°$, the converged RANS results show a definite slat wake, as depicted in Figs. 10(a) and 10(b).

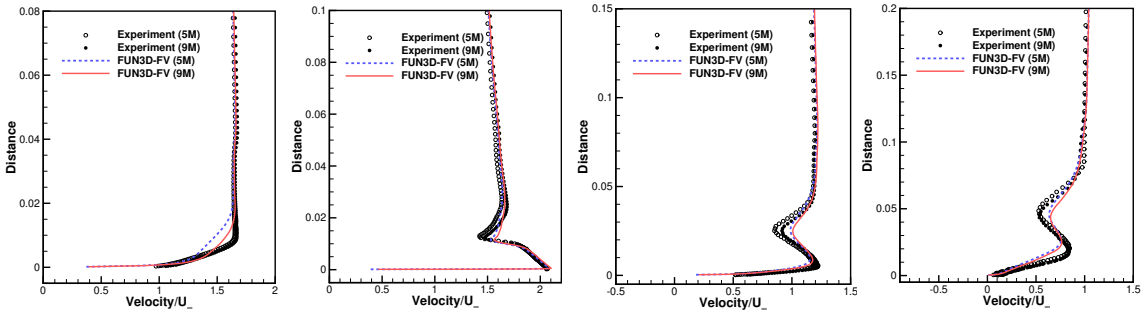

(a) $x/c = 0.45$ (b) $x/c = 0.8982$ (c) $x/c = 1.032$ (d) $x/c = 1.1125$

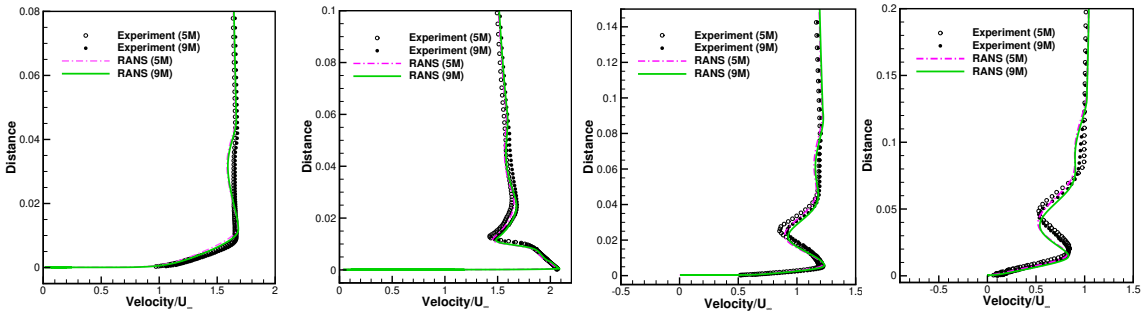

(e) $x/c = 0.45$ (f) $x/c = 0.8982$ (g) $x/c = 1.032$ (h) $x/c = 1.1125$

Fig. 7 Comparison of velocity profiles for 30P30N at 8 degrees. (a)–(d): WMLES; (e)–(h): RANS.

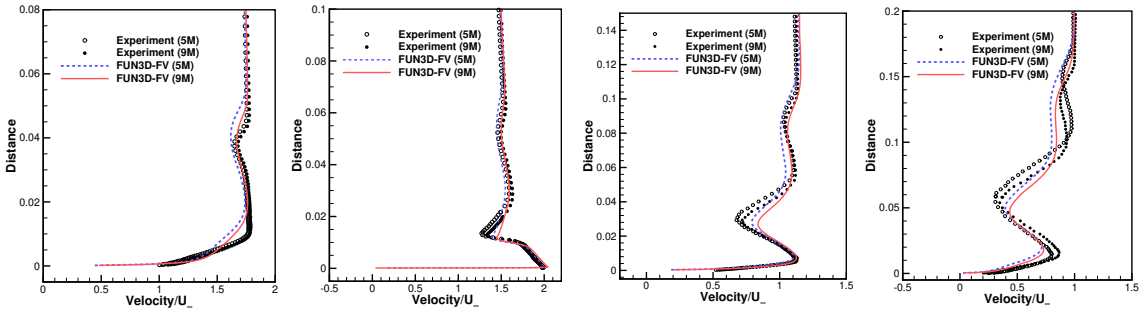

(a) $x/c = 0.45$ (b) $x/c = 0.8982$ (c) $x/c = 1.032$ (d) $x/c = 1.1125$

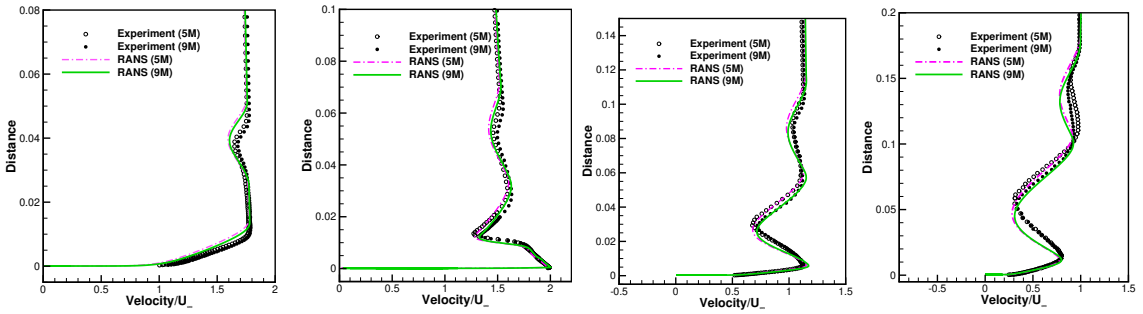

(e) $x/c = 0.45$ (f) $x/c = 0.8982$ (g) $x/c = 1.032$ (h) $x/c = 1.1125$

Fig. 8 Comparison of velocity profiles for 30P30N at 16 degrees. (a)–(d): WMLES; (e)–(h): RANS.

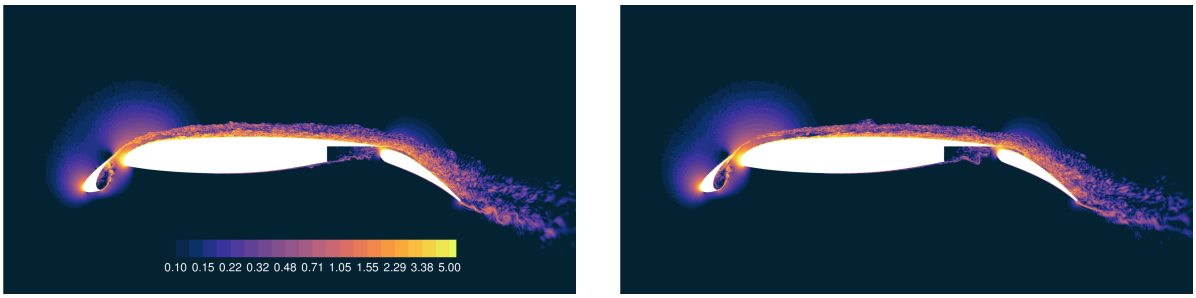

(a) Re = 5M, α = 8.12° (b) Re = 9M, α = 8.10°

(c) Re = 5M, α = 16.21° (d) Re = 9M, α = 16.21°

Fig. 9 Contours of instantaneous density-gradient magnitude around 30P30N for Reynolds numbers of 5M and 9M at 8- and 16-deg angles of attack computed by WMLES.

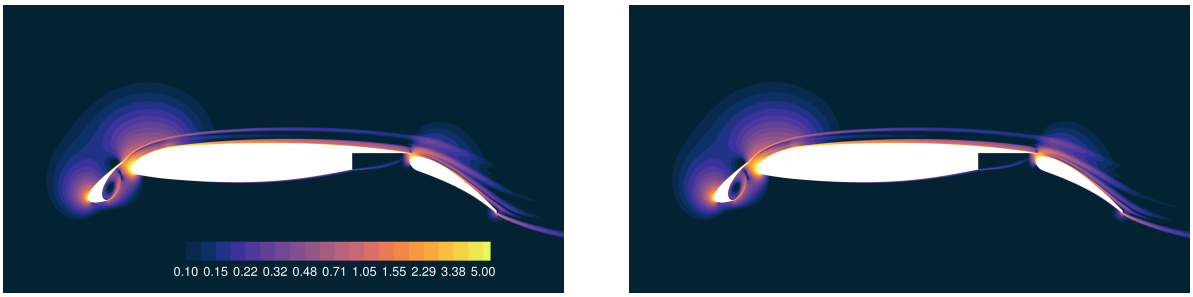

(a) Re = 5M, α = 8.12° (b) Re = 9M, α = 8.10°

(c) Re = 5M, α = 16.21° (d) Re = 9M, α = 16.21°

Fig. 10 Contours of density-gradient magnitude around 30P30N for Reynolds numbers of 5M and 9M at 8- and 16-deg angles of attack computed by RANS.

B. NASA High-Lift Common Research Model

In this section, WMLES results are presented for flows over the NASA CRM-HL model over a range of angles of attack, with the flaps in a landing configuration. The NASA CRM-HL configuration is a 10%-scale, semispan model that was tested in the QinetiQ 5-meter pressurized low-speed wind tunnel [38]. However, note that this configuration has been used in the CFD simulations at full scale, so all references to dimensional distances and locations herein refer to 100%-scale. This configuration incorporates many salient features of a realistic flight configuration, including a fuselage, a flow-through nacelle, nacelle pylon, nacelle chine, leading-edge slats, slat brackets, a main wing, trailing-edge flaps, and flap fairings. The experimental data were used for evaluating CFD simulations as part of the 4th AIAA CFD High Lift Prediction Workshop [5]. Free-air simulations are conducted for the nominal trailing-edge flap deflections of 40°/37° in the current work. More details about the geometry, test parameters, and related references are available from the workshop website [5].

1. Flow Conditions and Computational Grids

The flow conditions for this configuration are a freestream Mach number of 0.2, a Reynolds number of 5.49 million based on the mean aerodynamic chord (MAC) of 275.8" and a reference temperature of 521 °R. Results obtained by WMLES based on the FUN3D-FV and FUN3D-FE discretization methods are presented and compared with wall-corrected experimental data. A range of angles of attack have been considered in this study for $C_{L,max}$ predictions. The angles of attack in the FUN3D-FV computations conducted with WMLES include 7.05°, 11.29°, 17.05°, 19.57°, 20.55°, 21.47°, and 22.0°. Note that the angle of attack of 22.0°, which is an additional angle in the WMLES study, is not included in the wall-corrected experimental data set. The inclusion of this angle in the computations is purely to study the behavior of the integrated forces and pitching moment in the post-stall regime. The FUN3D-FE solver was used to perform WMLES at the angles of 7.05°, 17.05°, 19.57°, and 21.47°. All surface boundaries for the fuselage, slat, wing, flap, nacelle, etc. use the wall model for determining the surface shear stress. The outer boundary is located about 100 MAC lengths away, where farfield characteristic-type boundary conditions are imposed. A symmetry plane is located at $y = 0$.

In Ref. [6], WMLES solutions were assessed using the FUN3D-FV solver based on two unstructured grids, designated at the time as Mesh A and Mesh B. Meshes A and B contain approximately 419 million and 156 million grid points, respectively. Although generated independently, both grids have a nominal wall-normal spacing of 0.13", corresponding to a nominal $\Delta y_w^+ \approx 100$ based on a flat-plate approximation at freestream conditions and the MAC reference length. Along the surfaces of the slat, main wing, and flap, the grid points away from the leading and trailing edges are uniformly distributed. In the vicinity of the leading and trailing edges, clustering is used to improve accuracy in regions with large solution gradients.

In this paper, previously computed FUN3D-FV solutions obtained on Meshes A and B are included to compare with WMLES results obtained on a refined grid, referred to as Mesh A^+. The refined computational grid consists of approximately 555 million points and 1.12 billion mixed-type elements including hexahedra, tetrahedra, prisms, and pyramids. The nominal wall-normal spacing for Mesh A^+ corresponds to $\Delta y_w^+ \approx 100$. Because the first points off the wall are used in the present work as the exchange locations, generation of these computational grids has constrained the wall-normal spacing to meet the $\Delta y_w^+ \approx 100$ requirement to make the simple wall model [23] appropriate by placing a few points within the log layer. Compared to Mesh A, the total number of grid points on Mesh A^+ has increased by 32% and the number of surface points has increased by 45%. More details about the grid metrics are listed in Table 2:

A view of the entire surface mesh is not informative because the density of grid points is so high that no useful information can be visualized. Representative closeup views of the surface meshes in the vicinity of the fuselage are shown in Fig. 11. Figure 11(a) shows a closeup view of the surface of Mesh A^+ near the fuselage as indicated in Fig. 11(d). Figures 11(b) and 11(c) are the views of Meshes A and B, respectively, in the same region. For Mesh A^+, the trailing-edge region of the slat, the slat brackets, and the leading-edge region of the main wing have retained with the same grid density as that on Mesh A, while refinement by a factor of 2 has been performed in the streamwise and spanwise directions on the majority of the upper wing and flap surfaces. Specifically, both the streamwise and spanwise spacing on the surface elements of Mesh A^+ is about 0.25", whereas it is 0.5" for Mesh A. Hence, the ratio of wall-normal to streamwise spacing on the surface elements of Mesh A^+ is about 1:2. For Mesh B, the ratio of streamwise to spanwise spacing is nominally unity away from the leading and trailing edges. Near the leading and trailing edges, however, Mesh B has somewhat higher density as observed in Fig. 11 and this ratio remains approximately unity despite clustering. The ratio of wall-normal to streamwise spacing on Mesh B is about 1:5.

Figure 12 displays slices of Meshes A^+, A, and B at $y = 483.5$" that are representative of slices at the other stations.

Table 2 NASA CRM-HL Mesh Statistics.

Metrics	Mesh A^+	Mesh A	Mesh B
Vertices	555, 054, 821	418, 774, 938	156, 117, 308
tetrahedra	571, 031, 590	396, 153, 823	245, 076, 460
Pyramids	140, 454, 078	97, 054, 752	14, 799, 748
Prisms	2, 141, 281	1, 787, 526	215, 323, 499
hexahedra	408, 866, 245	317, 281, 293	0
Surface points	10, 815, 976	7, 418, 554	5, 011, 436
Surface triangles	210, 100	176, 232	9, 746, 096
Surface quadralaterals	11, 359, 927	7, 892, 108	168, 929
Nominal Δy_w^+	100	100	100

These figures provide views of the overall grid topologies, as well as point distributions near the surfaces of the main-wing cove and flap. Meshes A^+ and A are constructed using a layered approach, where the elements in each layer are roughly twice as large as the elements in the neighboring layer closer to the surface. The spacing in the wall-normal direction on Mesh A^+ is the same as that on Mesh A, but the streamwise spacing is reduced from 0.5" to 0.25". As a result, an ultrafine layer in the vicinity of the wall is formed on Mesh A^+, which can be observed by comparing Figs. 12(d) and 12(e). In the regions between the layers, Meshes A^+ and A employ tetrahedral and pyramidal elements to blend the layers. Mesh B uses mostly prisms for the boundary-layer cells and mostly tetrahedra away from the surface.

2. Solver Settings and Convergence

For FUN3D-FV, the simulations have been performed with 1,000–2,000 time steps per CTU and the time averaged quantities such as surface pressures and velocity components are collected over 8–15 CTUs after the transients in the forces and moments have been eliminated. Specifically, the time-step size for lower angle-of-attack cases corresponds to 1,000 time steps per flow-through pass, whereas 2,000 time steps per pass are selected for higher angle-of-attack cases ($\alpha \geq 19.57^\circ$) to increase temporal accuracy. The refinement for the time-step size is needed for resolving high-lift flows in the presence of increased unsteadiness, interactions of turbulent eddies of various scales, and flow separation. The implicit system of equations solved by HANIM [26] obtains 4–5 orders of magnitude in reduction of the root-mean-square residual norms using 6 subiterations for the problems presented here. The WMLES capability in the FUN3D-FV solver was initially implemented in central processing unit (CPU) kernels and has also been extended to graphics processing unit (GPU) enabled kernels. All FUN3D-FV simulations on Mesh A^+ presented in this section were performed using the NVIDIA V100 GPU nodes supported by the NASA Advanced Supercomputing (NAS) Division.

For the finite-element discretization, FUN3D-FE, all simulations have been performed using 1,000 time steps per CTU with two-stage implicit Runge-Kutta time stepping. At each time step, the nonlinear time-dependent residual is targeted for reduction of 5 orders of magnitude, although typically 6–7 are actually achieved due to rapid convergence as the pseudotime step increases across subiterations. For the linear system, 5 orders of magnitude are also achieved. Future work will be done to study the effects of various parameter settings on the solutions. The solutions obtained for the finite-element branch of FUN3D have all been obtained using the AMD Rome CPU nodes at the NAS facility. All FUN3D-FE solutions presented in this work are obtained on Mesh B. Here, the solutions at $\alpha = 19.57^\circ$ and 21.47° are initialized using FUN3D-FV results in an attempt to minimize solution time. Although not shown, this strategy has not been judged to save time in practice because the discretizations are different enough that strong transients are encountered upon restarting. As such, the solutions at $\alpha = 7.05^\circ$ and 17.05° have been obtained by starting from freestream.

Time histories of the integrated lift, drag, and pitching-moment coefficients computed on Mesh A^+ with FUN3D-FV and on Mesh B with FUN3D-FE are shown in Fig.s 13(a)–13(d) as a function of CTU for $\alpha = 7.05^\circ$, 17.05°, 19.57°, and 21.47°. The convergence histories from both solvers are shown for the last 5–10 CTUs toward the end of each simulation that are used to establish statistics of the quantities of interest. Note that in general, 30–50 CTUs are simulated before time averages are collected, although more flow-through passes may optionally be used to examine

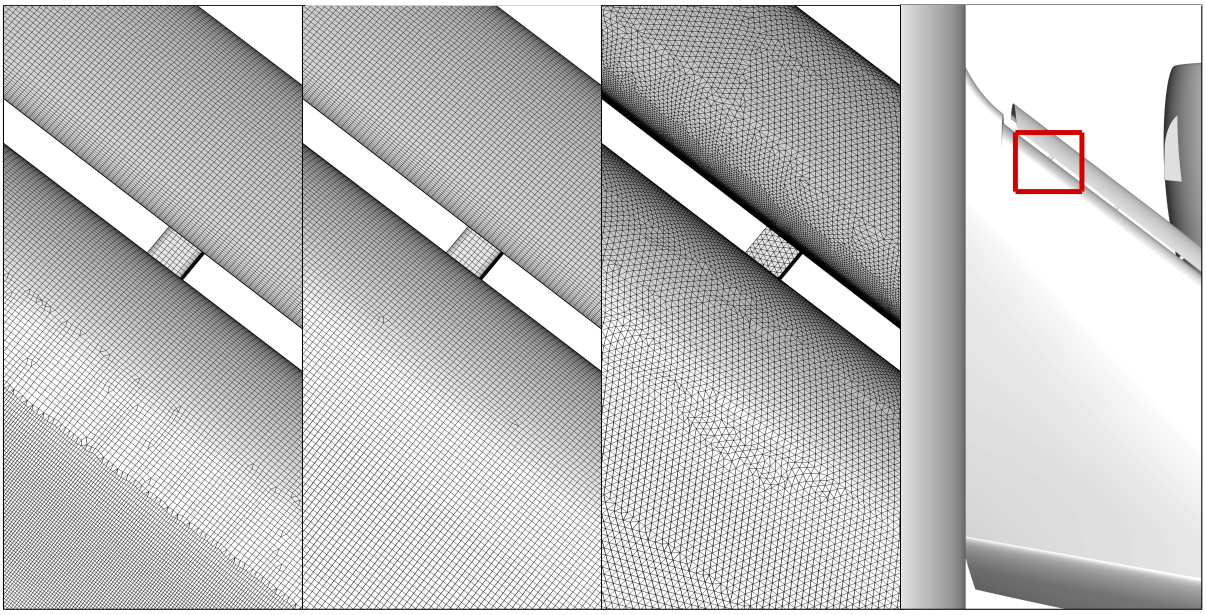

(a) Mesh A$^+$ (b) Mesh A (c) Mesh B (d) Location for closeup view

Fig. 11 NASA CRM-HL surface mesh near fuselage.

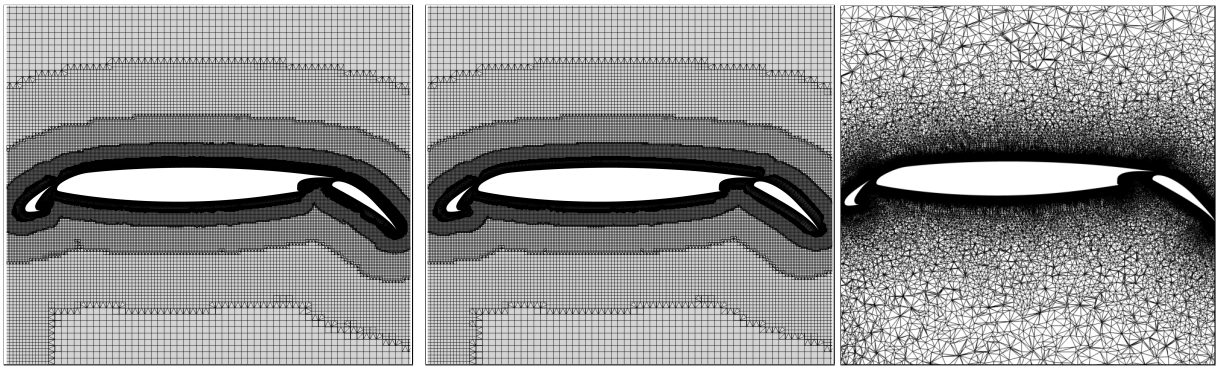

(a) Mesh A$^+$: wing-section view (b) Mesh A: wing-section view (c) Mesh B: wing-section view

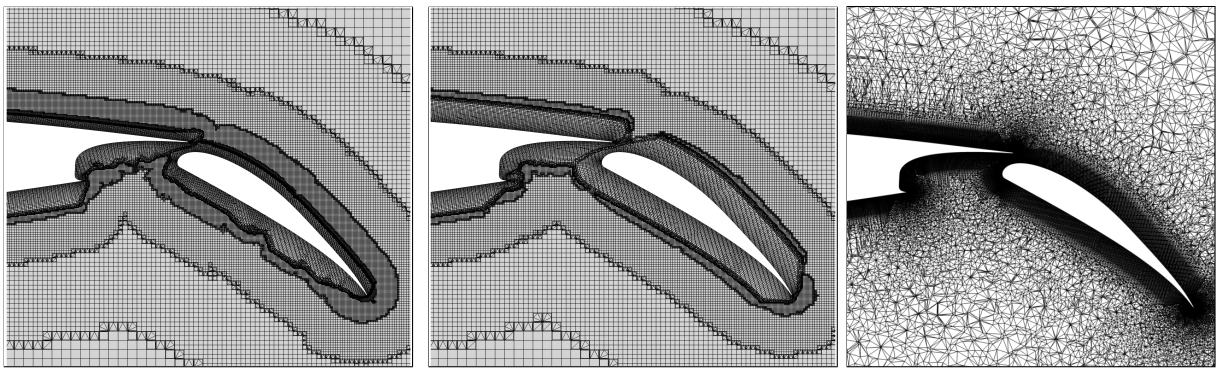

(d) Mesh A$^+$: flap view (e) Mesh A: flap view (f) Mesh B: flap view

Fig. 12 NASA CRM-HL mesh slices at $y = 483.5$" near wing midspan.

any transient effects, especially at the highest angles of attack. All WMLES computations in this work have been performed with sufficiently long integration time to be reasonably converged. One final note is that for the time averages of the finite-element simulations, the skin friction from the wall model had not been included for the pitching moment calculations, although it had been included for both lift and drag. Subsequent calculations at each angle of attack indicate that the differences in pitching moment due to inclusion of this contribution are between 0.5% and 1.8%. It is observed that the lift, drag, and pitching moment coefficients have become sufficiently stationary in all the simulations. An interesting observation, seen by comparing the finite-volume and finite-element results, is that the FUN3D-FV results appear to produce higher frequency and higher amplitude oscillations in the time history profiles than FUN3D-FE. The more oscillatory time-dependent features associated with the FUN3D-FV convergence could be caused by different levels of convergence in the nonlinear system in these two solvers, but in this case are likely caused by the different grid spacings and topologies between Meshes A^+ and B. Although not shown, FUN3D-FV computations on Mesh B show similar convergence characteristics as the FUN3D-FE solver on the same grid as shown in Fig. 13. Results obtained during the workshop [5] depict various convergence characteristics depending on the participant; further investigations will be needed to attain better understanding of the convergence behavior. The convergence histories for $\alpha = 22.0^\circ$, computed on Mesh A^+ with FUN3D-FV, are shown in Fig. 13(e). An interesting observation in this case is that the integrated lift, drag, and pitching-moment coefficients appear to become stationary in the range of 50–65 CTUs; however, noticeable changes occur after 65 CTUs where the drag starts to increase considerably together with more negative pitching moment. The longer required time integration at higher angles could be caused by the increased interactions among various geometrical components (e.g., wing and nacelle) or with the fuselage, which has a convective length of 9 times more than the MAC of the wing. The presented 21.47° computations by FUN3D-FV have also been conducted about 80 CTUs but such sudden variations appearing in the 22.0° case do not occur.

3. Force and Moment Results

Integrated forces and moments computed by free-air FUN3D-FV WMLES on Meshes A^+, A and B, and FUN3D-FE on Mesh B are depicted in Fig. 14; the wall-corrected experimental measurements are also plotted as references. Note that the FUN3D-FV results on Meshes A and B were previously described in Ref. [6].

Figure 14(a) shows computed lift coefficients versus the angle of attack. For the $\alpha = 7.05^\circ$ case, the lift coefficients predicted on Mesh A^+ by FUN3D-FV and on Mesh B by FUN3D-FE show good agreement with each other and with the experimental data. At $\alpha = 11.29^\circ$, where the lift curve is approximately linear, WMLES computations by FUN3D-FV on all three grids continue to exhibit good agreement with the experiment. The difference between the computed lift coefficient on Mesh A^+ and the experiment becomes smaller at this angle of attack than the $\alpha = 7.05^\circ$ case. At $\alpha = 17.05^\circ$, the lift coefficient computed on Mesh A using FUN3D-FV is below that of the experimental data by approximately 3.2%. However, the lift prediction computed on Mesh A^+ by FUN3D-FV has significantly improved, showing only a small 0.5% difference compared to the experiment. More discussions about this improved lift prediction are given later. The WMLES solutions obtained by FUN3D-FE on Mesh B for this angle of attack match the experimental data very well, showing a small 0.6% deviation from the experimental data. At $\alpha = 19.57^\circ$ near the experimental $C_{L,max}$, WMLES computations conducted by FUN3D-FV on Meshes A^+ and A as well as FUN3D-FE on Mesh B accurately predict the critical angle of attack for $C_{L,max}$, and the differences in the lift coefficients are within 1% from the measurements for both solvers.

For the post-stall cases, the WMLES lift prediction obtained using FUN3D-FV on Mesh A^+ at $\alpha = 20.55^\circ$ consistently shows an improvement compared to that obtained from the initial grid (Mesh A). At the highest angle of attack, corresponding to $\alpha = 21.47^\circ$, results from both FUN3D-FV on Mesh A^+ and FUN3D-FE on Mesh B exhibit higher lift than the experiment. This discrepancy between the simulations and the experimental results could be caused by the fact that the present simulations are performed in free air without accounting for tunnel-wall effects present in the experiments. Nonetheless, both FUN3D-FV and FUN3D-FE solvers show good capabilities of evaluating the lift forces and capturing the flight characteristics for this high-lift configuration including maximum lift predictions. At $\alpha = 22.0^\circ$ conducted with FUN3D-FV on Mesh A^+, the computed lift coefficient agrees very well with the wall-corrected experimental data corresponding to $\alpha = 21.47^\circ$.

Figures 14(b) and 14(c) show the experimental and computed drag polars versus the angle of attack and the lift coefficient, respectively. The WMLES results on Mesh A^+ by FUN3D-FV and Mesh B by FUN3D-FE closely follow the experimental drag-polar curve in almost all flow regimes, including the linear regime at lower angles of attack, the angle of attack near the experimental $C_{L,max}$, and post-stall. Improved agreement has been attained by the FUN3D-FV solver on the refined Mesh A^+ versus the original Mesh A: the drag predictions on Mesh A^+ at $\alpha = 17.05^\circ$ and $\alpha = 20.55^\circ$

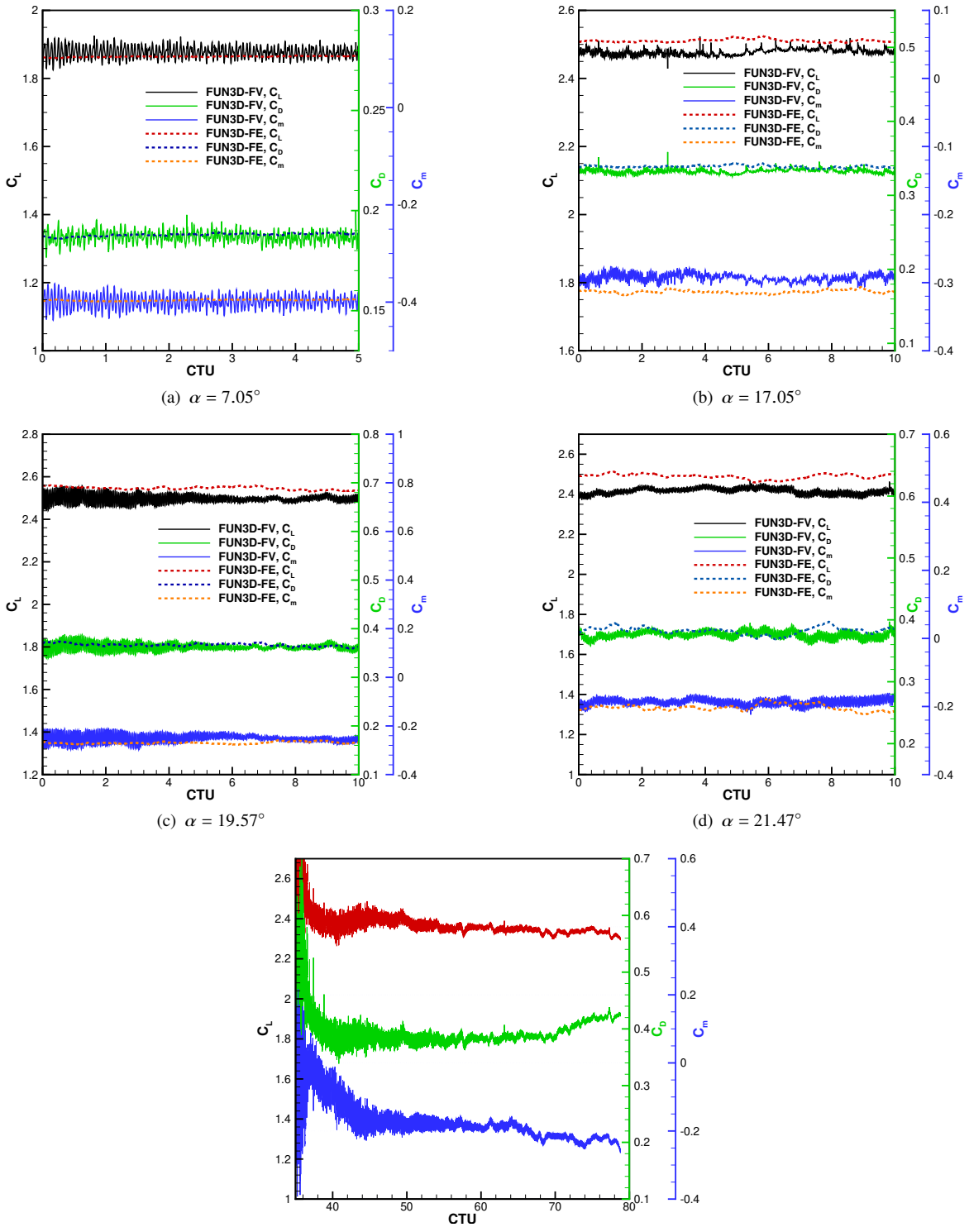

(a) $\alpha = 7.05°$

(b) $\alpha = 17.05°$

(c) $\alpha = 19.57°$

(d) $\alpha = 21.47°$

(e) $\alpha = 22.00°$, FUN3D-FV

Fig. 13 Convergence histories of lift, drag, and pitching moment coefficients in the last 5–40 CTUs of WMLES computations.

show enhanced agreement with the measurements with only 0.2% and 1% differences, respectively. Similarly, the FUN3D-FE solver exhibits accurate drag predictions at almost all angles of attack, except for the highest angle of attack,

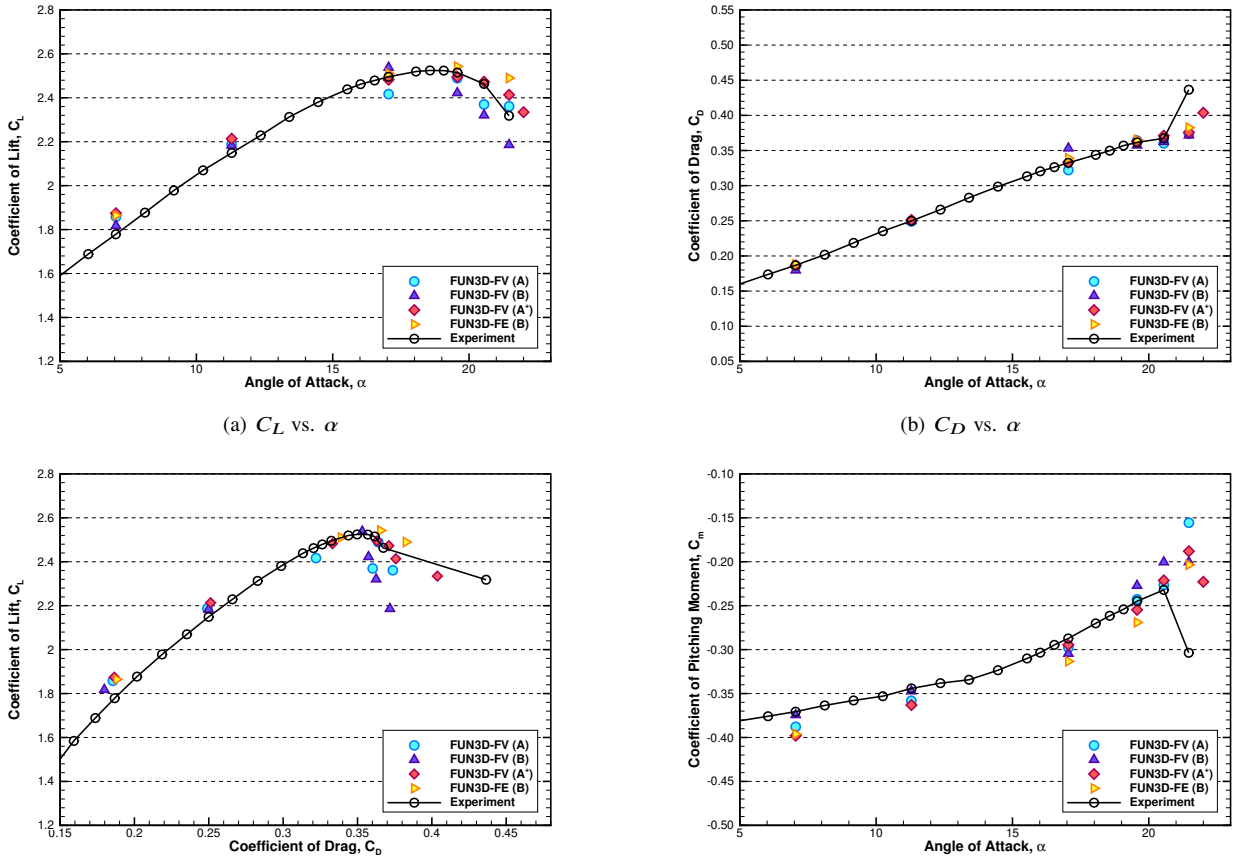

(a) C_L vs. α

(b) C_D vs. α

(c) C_L vs. C_D

(d) C_m vs. α

Fig. 14 Polar profiles obtained by WMLES for CRM-HL configuration.

$\alpha = 21.47°$, where the drag coefficients computed on both FUN3D-FE and FUN3D-FV are underpredicted compared to the experiment. At $\alpha = 22.0°$, significant improvements in the drag polars are observed by comparing the computed FUN3D-FV WMLES solutions with the experimental curves. The differences in the drag prediction at the higher angles of attack could be a result of the lack of tunnel-wall effects, where the computed flow separation near the wing-root is not at the same extent as that in the experimental study.

Figure 14(d) shows the pitching-moment coefficients versus angle of attack. At all angles of attack except for $\alpha = 21.47°$, the WMLES computations obtained by FUN3D-FV on Mesh A^+ show good agreement with the experimental data. The maximum difference corresponding to $\alpha = 7.05°$ is about 7.4%, which is somewhat higher than the result obtained originally on Mesh A (4.7% deviation). The difference in the pitching moments corresponding to the critical angle of attack at $\alpha = 19.57°$ is within 0.9%. At the highest angle of attack, $\alpha = 21.47°$, the agreement on the pitching moment on Mesh A^+ shows an improvement compared to the result on Mesh A; however, its magnitude is still not negative enough as compared to the experimental data, which indicates a strong nose-down pitching moment, referred to as a pitch break. At $\alpha = 22.0°$, the pitch-break phenomenon is predicted by FUN3D-FV WMLES on Mesh A^+, where the rapid change in the pitching moment as that shown in the experiment is successfully captured. The FUN3D-FE solver on Mesh B shows reasonably good predictions on the pitching moments at $\alpha = 7.05°$, $\alpha = 17.05°$, and $\alpha = 19.57°$. At $\alpha = 19.57°$, the difference in the pitching moment computed by FUN3D-FE is about 5% as compared to experiment. However, as mentioned previously, this time-averaged value did not include contributions from skin friction. Subsequent comparisons at a few individual time steps indicate that the pitching moment would increase by approximately 1.4% with the inclusion of skin friction, thereby reducing this difference to within 3.6%. As with the other results, at $\alpha = 21.47°$, the computed pitching moment coefficient by FUN3D-FE does not indicate a sudden nose-down tendency. Note that for all angles of attack, the results obtained using FUN3D-FE more closely agree with FUN3D-FV results obtained on Meshes A and A^+ than they do with FUN3D-FV results obtained on Mesh B.

4. Surface Pressure Distributions

Figure 15 displays the locations of spanwise slices (A–H) where experimental data are available for CFD validation; slices highlighted in red (i.e., A, D, E, and G) are stations at which computed results are compared with experiments in this paper to examine the WMLES capabilities in capturing key aerodynamic characteristics for high-lift systems. Results are shown at these selected stations to conserve space. In Figs. 16–19, computed pressure distributions are compared with experimental data at four angles of attack, $\alpha = 7.05°$, $17.05°$, $19.57°$, and $21.47°$.

Figure 16 shows pressure distributions computed on Meshes A^+, A, and B for $\alpha = 7.05°$. As described previously, the FUN3D-FV solver performed WMLES computations on all three meshes, while the FUN3D-FE solver performed WMLES only on Mesh B. At all spanwise stations, the computed pressure distributions are in overall good agreement with each other and the experimental data. Pressure distributions computed on Mesh A^+ exhibit small oscillations near the slat leading edge at most of the spanwise stations. Querying the skin friction indicates that these locations correspond to the flow transition from a smooth state to an oscillatory one. The agreement on the flap suction side on Mesh A^+ has clearly improved at stations A, D, and E when compared to those obtained on Mesh A. This is likely due to the enhanced surface mesh resolution on Mesh A^+. Compared to the experimental data, the FUN3D-FE solver displays good agreement on the pressure distribution at all stations, as compared to both the experimental data and the FUN3D-FV results. Small pressure oscillations are observed on the flap suction side near the midchord in the FUN3D-FE results, which appear with smaller magnitude inboard, progressively increasing toward the wing midspan, and then vanishing near the wingtip.

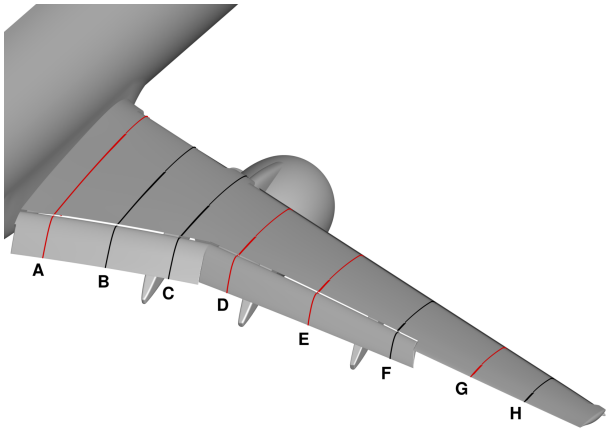

Fig. 15 Slice locations for NASA CRM-HL experimental data.

Figures 17 and 18 show pressure distributions at $\alpha = 17.05°$ and $\alpha = 19.57°$, respectively. At $\alpha = 17.05°$, as discussed previously, the integrated lift coefficient computed by FUN3D-FV on Mesh A^+ has shown an improvement compared to the initial result on Mesh A (Fig. 14(a)). This improvement is reflected by the better agreement on the flap suction sides at stations A and B; pressures at the latter station are shown at the end of this section for consistent presentation of the four representative stations. Better agreement is also observed near the suction peak of the slat at stations D and E. Note that at station A, the pressures obtained using FUN3D-FV on Mesh A^+ and those obtained using FUN3D-FE on Mesh B agree closely. However, also note that at stations D and E, both FUN3D-FV and FUN3D-FE exhibit the small hump in the pressure distributions at approximately midchord on the suction side of the flap.

At $\alpha = 19.57°$, the pressure distributions at various stations obtained by FUN3D-FV on Meshes A^+ and A are in close agreement except for small improvements observed on Mesh A^+ in capturing the pressures on the suction side of the flap at stations D and E. At the most inboard spanwise location (Station A), the pressure distributions on the flap computed on Mesh B by FUN3D-FV show better agreement with the experiment than the results from Meshes A^+ and A by FUN3D-FV as well as on Mesh B by FUN3D-FE, although all other WMLES pressure distributions agree among each other very well. The reasons for the differences at Station A are currently not known and more analysis is required. For this purpose, examining experimental data on the fuselage itself may be useful. Note that in Fig. 18, the pressure distributions computed on both Meshes A^+ and A show oscillations on the slat at the most inboard spanwise location, but the oscillations gradually lessen outboard. Similarly, small oscillations shown near the flap suction peaks on Mesh A at all stations continue to be visible in the results on Mesh A^+. In contrast, the pressure distributions computed on Mesh B exhibit small oscillations on the slat at all the spanwise locations and also exhibit

noticeably "wavy" solutions at stations E and G. In terms of the FUN3D-FE results for $\alpha = 19.57°$, the agreement with the experiment and the FUN3D-FV solutions is generally good; however, the "wavy" features on the slat suction side are also observed. An examination of the flowfield in this vicinity indicates that the majority of the slat upper surface in the FUN3D-FE solutions appears to remain laminar without transitioning to turbulence.

At $\alpha = 21.47°$ shown in Fig. 19, noticeable differences between the computed pressure distributions and the experiments are observed on the slat at Station A. The suction peak of the main wing at this station also appears to be overpredicted. The overpredicted pressures on the suction sides of the slat and the main wing near the wing root indicate that the flow separation in the simulations is not as strong as that observed in the experiments. At Station A, the pressure distributions near the trailing edge of the main wing and on the flap upper surface on Mesh A^+ indicate somewhat more lift than that computed on Mesh A. This difference contributes to higher nose-down pitching moment produced on Mesh A^+ in inboard regions. The pressure distributions computed on Mesh B by FUN3D-FE continue to show qualitatively consistent results as compared to the WMLES solutions by FUN3D-FV on Meshes A^+ and A. However, as will be demonstrated shortly, the flow on the slat again remains largely laminar.

As discussed previously, at $\alpha = 17.05°$, the WMLES solution on Mesh A^+ has shown better agreement on the computed lift coefficient than the original solution on Mesh A (cf. Fig. 14(a)). Querying the flowfield yields the observation that the nacelle wake at this angle of attack appears to interact more with the upper wing surface downstream of the nacelle. Hence, in addition to Fig. 17 showing the pressure distributions at stations A, D, E, and G, the pressure distributions at Station B is provided and shown in Fig. 20 because this station is located approximately inline with the flowfield from the nacelle. It is evident that the flap suction peak is much more accurately captured on Mesh A^+ with the surface mesh refinement, as well as the surface pressures near the flap trailing edge. Noticeable improvements are also seen on the suction sides of the slat and the main wing. Another interesting observation is that the surface pressure coefficients gradually become more negative near the trailing-edge of the wing and show better agreement with the experiments than the pressures computed on Mesh A.

Figure 21 shows comparisons of surface pressures at stations A and B for FUN3D-FV WMLES computations on Mesh A^+ at $\alpha = 22.0°$; note that the computed results on Meshes A and B by FUN3D-FV as well as the wall-corrected experiment data in this figure correspond to $\alpha = 21.47°$ and are included for references. Compared to the FUN3D-FV results at $\alpha = 21.47°$ on Meshes A, B, and A^+ (cf. Fig. 19(a))), significantly improved agreement on the computed surface pressures at the suction sides of the slat and main wing is obtained in the case of $\alpha = 22.0°$. Changes in the pressures at all other stations are negligibly small and thus are not included in the paper.

5. Flowfield Visualizations

Contours of time-averaged skin-friction coefficient magnitude and time-averaged streamlines are shown in Figs. 22 and 23, respectively, for $\alpha = 7.05°$, $17.05°$, $19.57°$, and $21.47°$, obtained on Mesh A^+ by the FUN3D-FV WMLES approach. It is clearly observed that as the flow angle of attack increases, the separation regions on the wing suction side increase substantially near the wing root as well as on the upper wing surface downstream of the nacelle, shown by the enlarged darker areas in Figs. 22(a)–22(d). The separation in the outboard regions initiated by the slat bracket wakes has also become larger with increasing the angle of attack. However, it is important to note that no significant separation occurs on the outboard part of the wing at any of the angles of attack, including the one corresponding to $C_{L,max}$ and ones in the post-stall regime. The wedge-shaped separation [39] commonly observed in RANS solutions as a result of excessive outboard separation is not encountered in these WMLES computations. The capability of the WMLES approach for capturing the correct flow structures across a large range of test conditions for high-lift systems has made the approach particularly valuable. Moreover, the slat bracket wakes are clearly shown in all the cases in Fig. 22 and the strengths appear to enhance with higher angles of attack. The observation of flow topology and patterns at different angles of attack can be further made by considering the time-averaged streamlines shown in Fig. 23. Here, a consistent trend of increased flow separation in the wing-root and outboard areas is shown. Additionally, separation near the leading edge of the nacelle is observed when approaching the angle of attack near $C_{L,max}$ and beyond; however, uncertainties regarding the nacelle separated flow can be raised due to tripping in the experiments that is not accounted for in the numerical simulations.

Instantaneous isosurfaces of Q-criterion computed by FUN3D-FV on Mesh A^+ and by FUN3D-FE on Mesh B are shown in Fig. 24 for the post-stall angle of attack of $\alpha = 21.47°$, colored by instantaneous streamwise velocity. Here, the WMLES computations based on the finite-volume and finite-element approaches in FUN3D deliver qualitatively similar flowfields, even though the results obtained using the finite-element approach have been obtained on the smaller grid, Mesh B. The two methods successfully capture fine turbulent structures and propagate them downstream close to

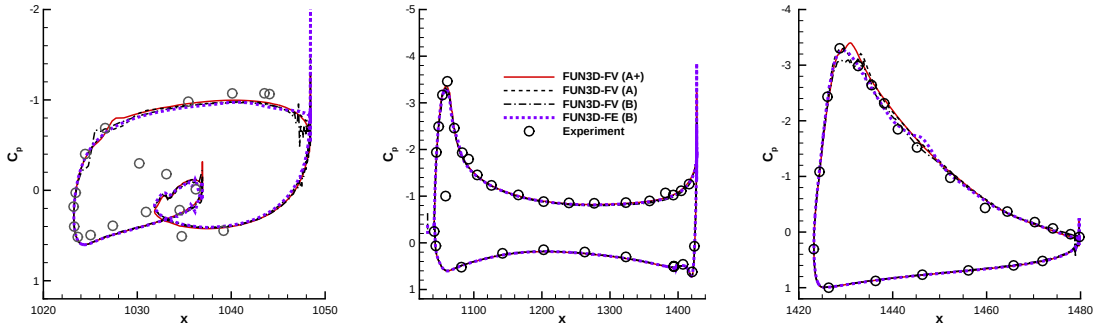

(a) Station A

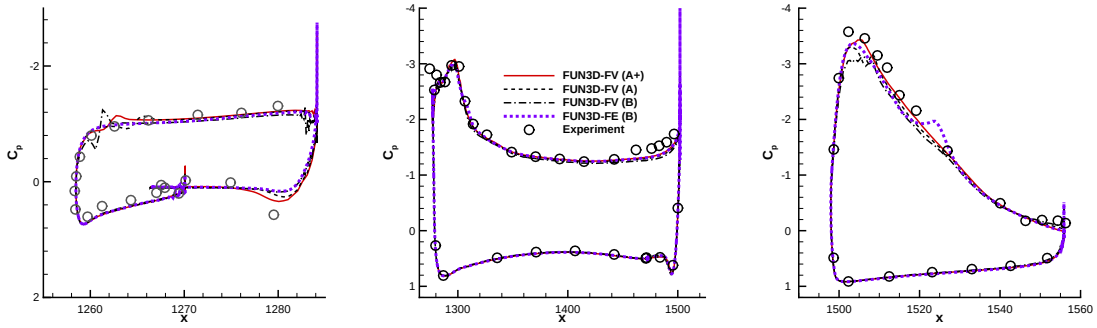

(b) Station D

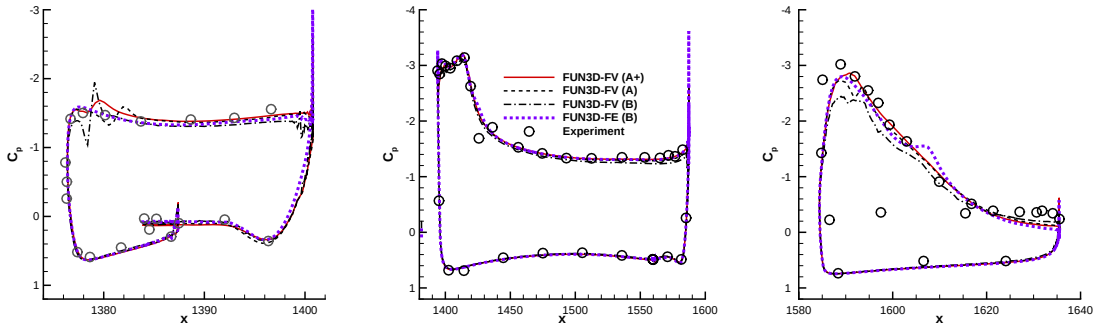

(c) Station E

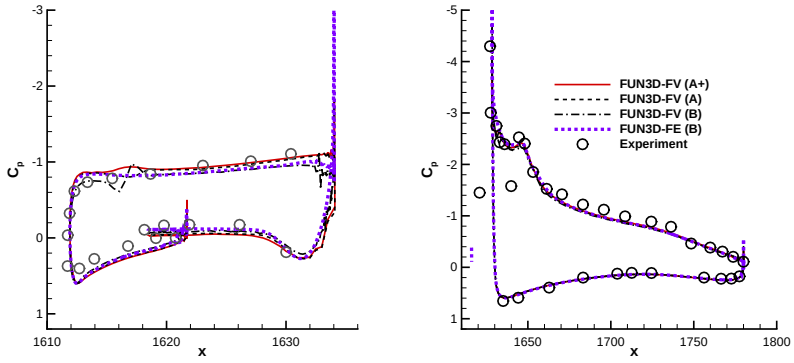

(d) Station G

Fig. 16 NASA CRM-HL pressure distributions at four spanwise stations: $\alpha = 7.05°$**.**

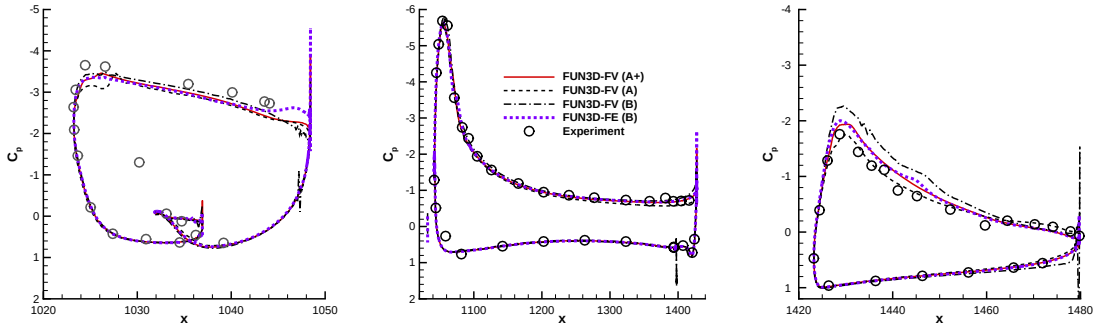

(a) Station A

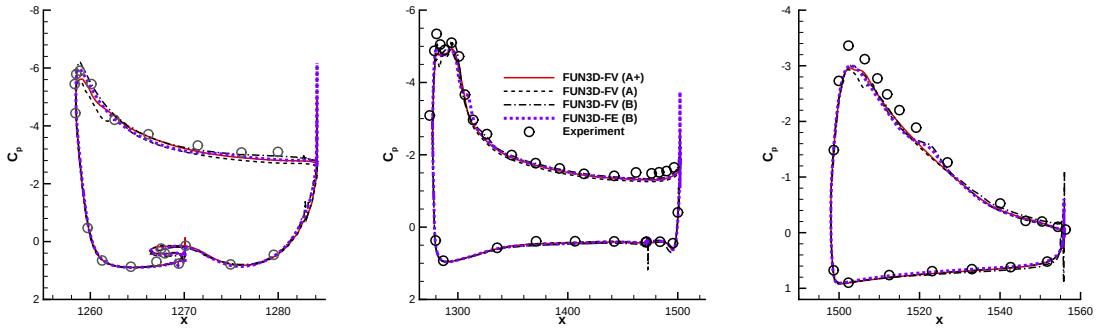

(b) Station D

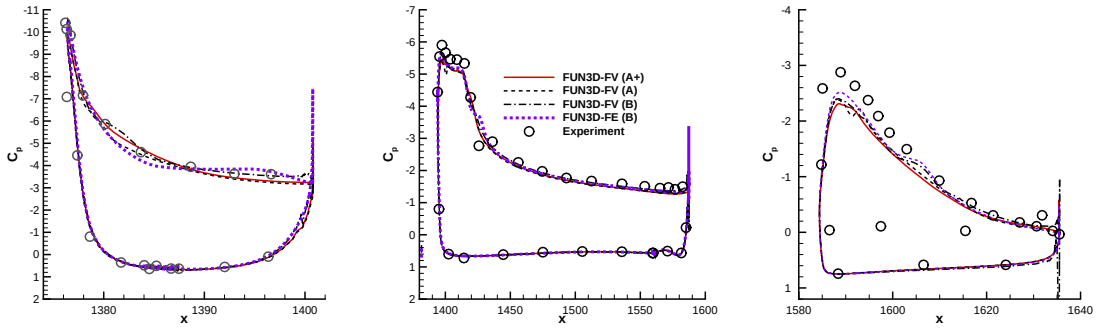

(c) Station E

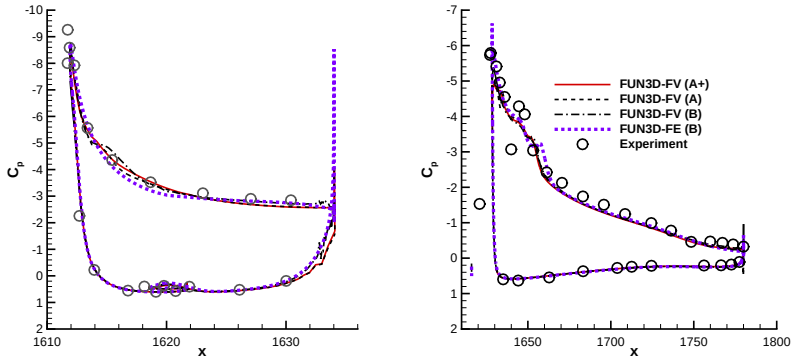

(d) Station G

Fig. 17 NASA CRM-HL pressure distributions at four spanwise stations: $\alpha = 17.05°$**.**

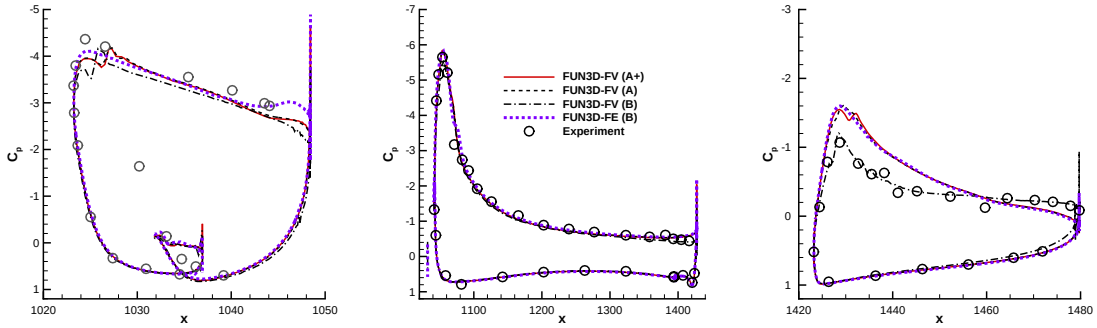

(a) Station A

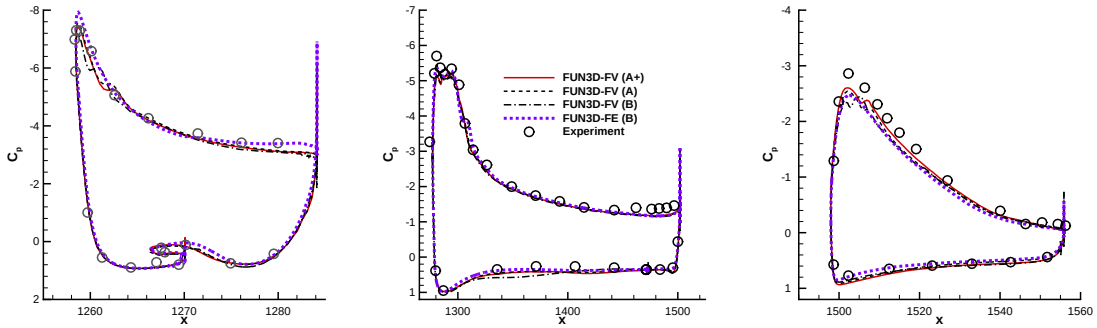

(b) Station D

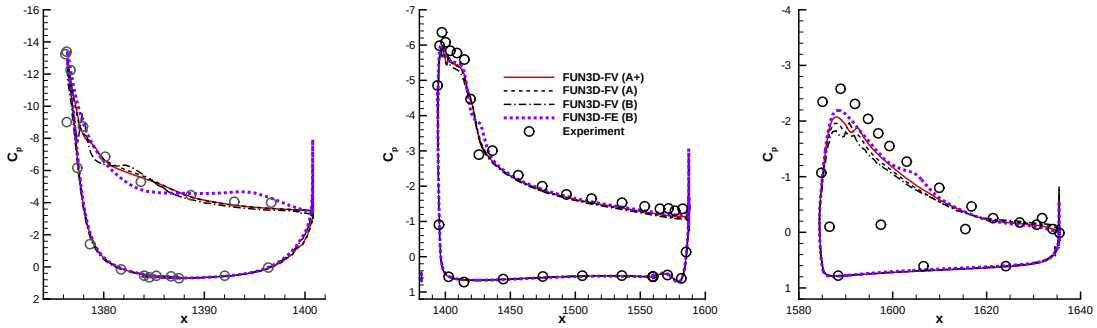

(c) Station E

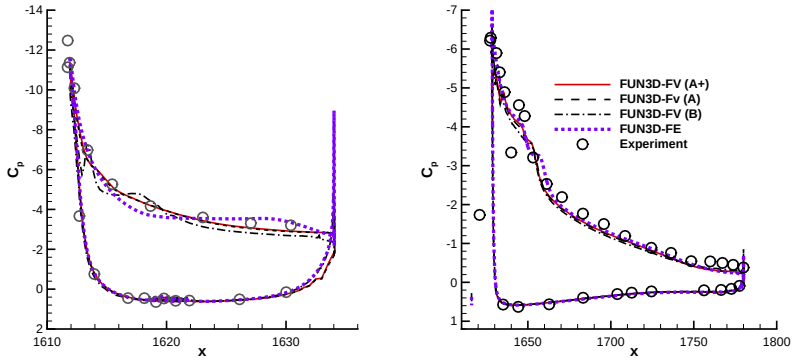

(d) Station G

Fig. 18 NASA CRM-HL pressure distributions at four spanwise stations: $\alpha = 19.57°$**.**

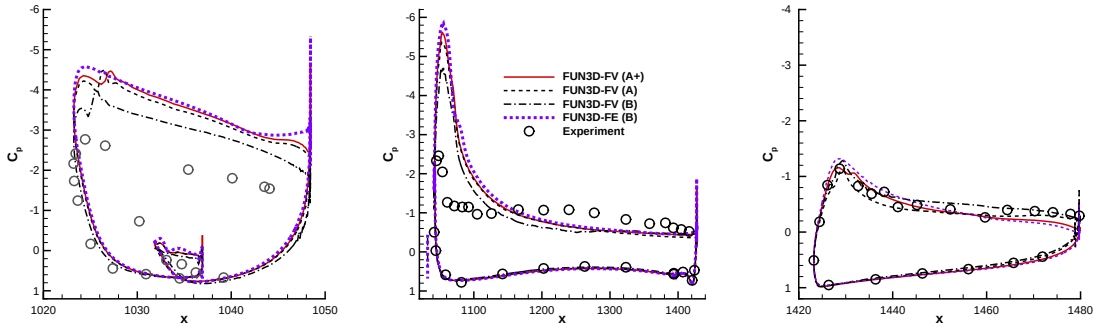

(a) Station A

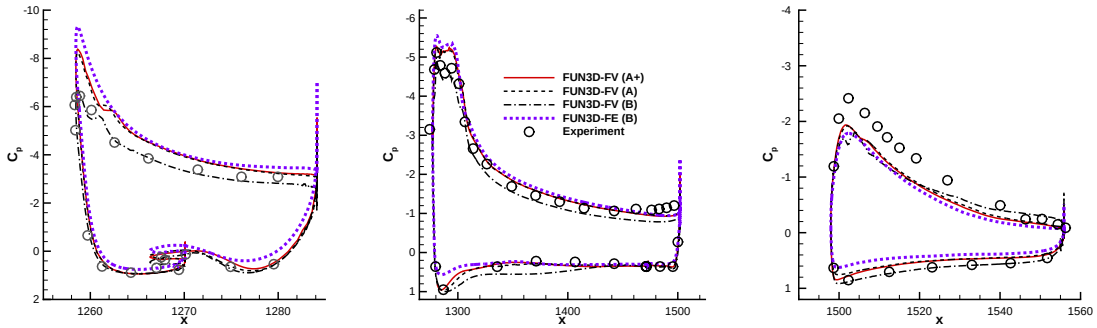

(b) Station D

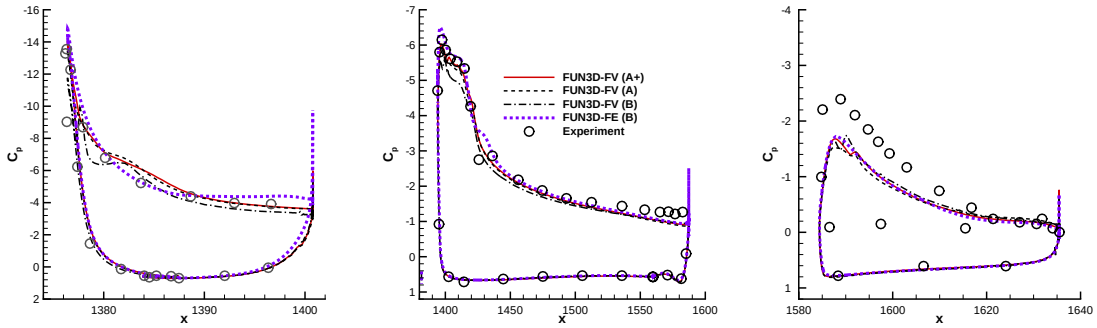

(c) Station E

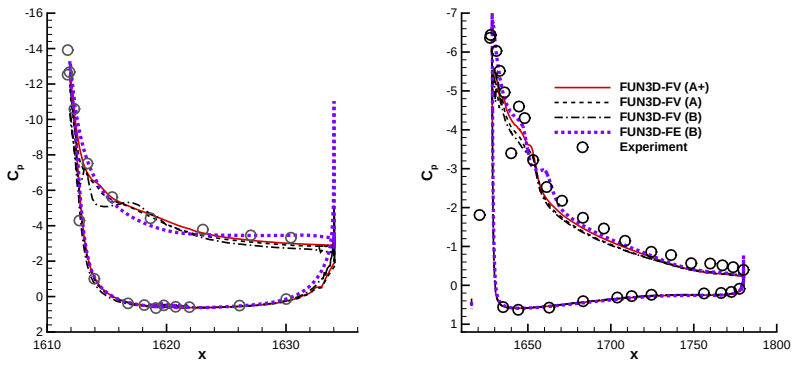

(d) Station G

Fig. 19 NASA CRM-HL pressure distributions at four spanwise stations: $\alpha = 21.47°$.

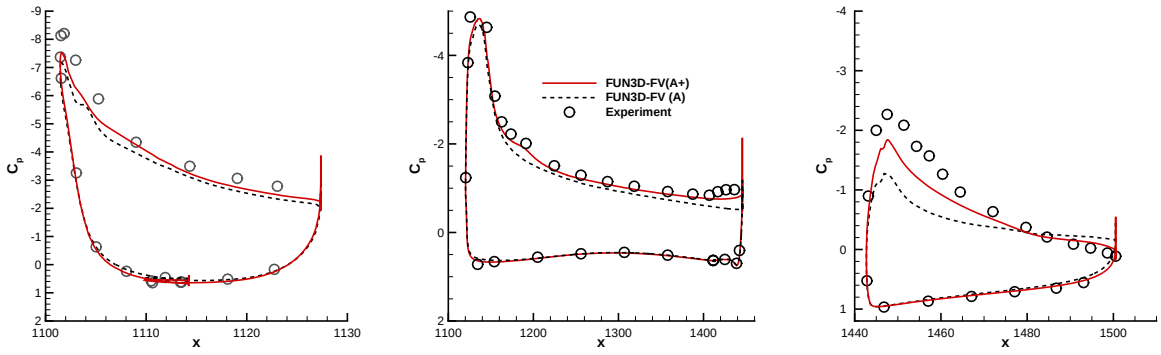

Fig. 20 NASA CRM-HL pressure distributions at Station B: $\alpha = 17.05°$.

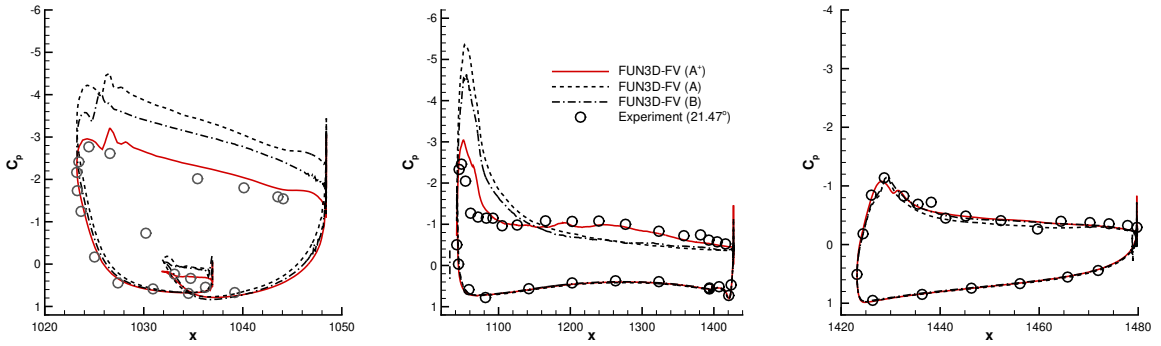

(a) Station A

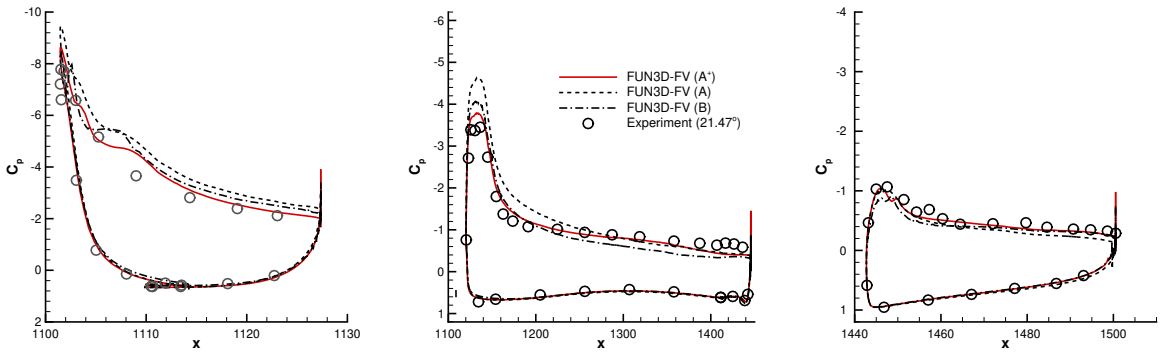

(b) Station B

Fig. 21 NASA CRM-HL pressure distributions at Stations A and B: $\alpha = 22.0°$. Experimental data correspond to wall-corrected data at $\alpha = 21.47°$.

the wing/fuselage surface. Complicated vortical structures of various scales are observed near the wing-root juncture region, the inboard slat, and the nacelle chine and nacelle/pylon. These geometrical features shed vortices and turbulent eddies that propagate over the inboard wing and fuselage areas. The vortices generated from the slat brackets seem to be mild in strength as compared to other vortical systems. Despite the similarities, there are also a few differences observed between the FUN3D-FV and FUN3D-SFE solutions shown in Fig. 24: (1) the instantaneous velocity field on the fuselage computed by FUN3D-FV on Mesh A^+ appears to show some oscillations, whereas the solution obtained by FUN3D-FE is shown to be somewhat smoother. However, a further investigation of the time-averaged velocity field does not exhibit any oscillations. Hence, this small difference on the fuselage velocity could be due to the different

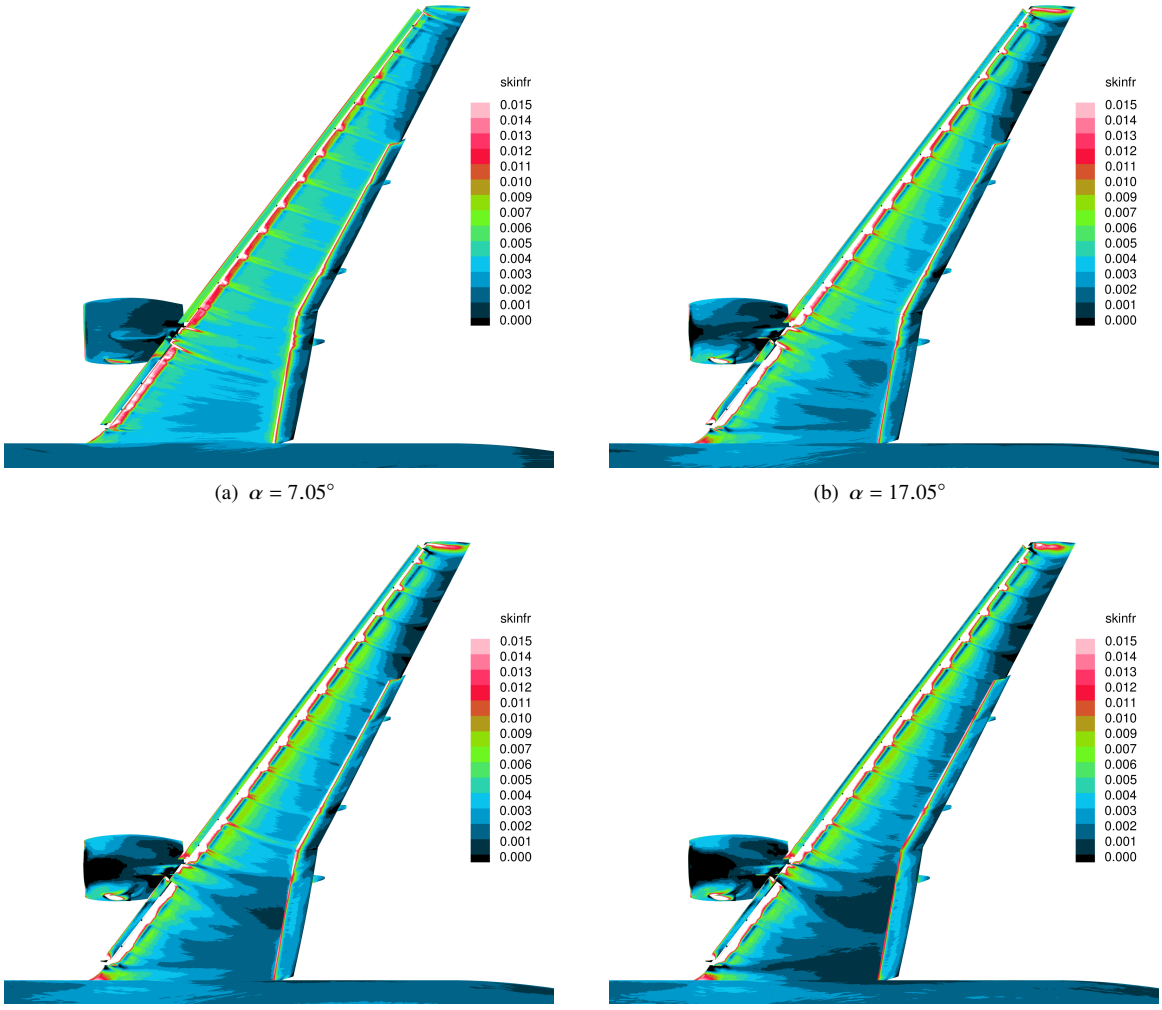

(a) $\alpha = 7.05°$ (b) $\alpha = 17.05°$

(c) $\alpha = 19.57°$ (d) $\alpha = 21.47°$

Fig. 22 Contours of time-averaged skin frictions on CRM-HL configurations at various angles of attack computed by FUN3D-FV on Mesh A^+.

time instances associated with the isosurface figures; and (2) the FUN3D-FE solution indicates that the flow on the slat suction side does not appear to transition to turbulence, as shown by the lack of resolved turbulent eddies and fluctuations on the slat (Figs. 24(a) versus 24(b)). This difference could be caused by different grid resolution or different numerics in the WMLES computations.

Finally, Figs. 25–27 show contours of instantaneous density-gradient magnitude computed by FUN3D-FE on Mesh B, and FUN3D-FV on Meshes A^+ and B for $\alpha = 21.47°$ at four stations, namely stations A, C, E, and H. The surface contours are colored by time-averaged pressure. Qualitative agreement on the flowfield structures between the WMLES solutions by the two discretization methods is again achieved. At the most inboard station (Station A), shedding vortices are seen to be generated at the leading and trailing edges of the slat, wing, and flap, interact with each other, and form an extensive wake region behind the wing. On Mesh A^+, the increased grid resolution becomes beneficial for the FUN3D-FV solver to capture much smaller and intense turbulent scales than those appearing in the results on Mesh B. Nonetheless, comparing the solutions obtained on Mesh B by the two discretization methods arrives at the observation that the present finite-element method better preserves and propagates small-scale flow features and various wake structures downstream of the vehicle. At Station C, where the cut-plane is near the middle of the nacelle, vortices are created from the leading edge of the nacelle, and then the nacelle wakes travel mostly over the upper surface of the

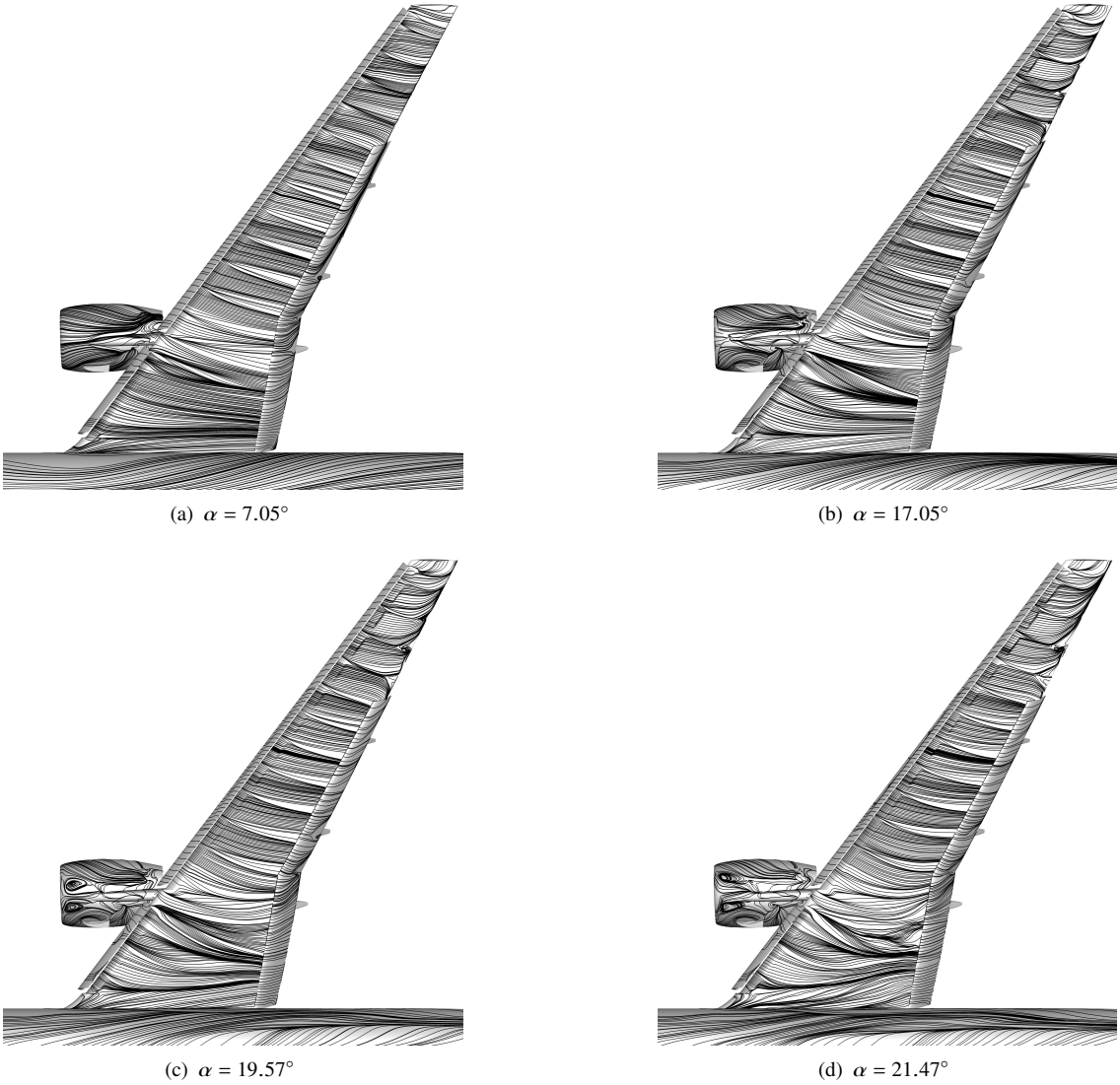

(a) α = 7.05°

(b) α = 17.05°

(c) α = 19.57°

(d) α = 21.47°

Fig. 23 Time-averaged streamlines on CRM-HL configurations at various angles of attack computed by FUN3D-FV on Mesh A$^+$.

nacelle/pylon and finally compress after reaching the leading edge of the wing. Moving to the outboard stations in closeup views for stations E and H, the slat wake can be observed, which propagates across the main wing and goes all the way to the flap (e.g., Fig. 26(d)), and enhanced interactions between the slat wake and turbulent boundary layer are observed. Moreover, because of the reduced chord length toward the wingtip, shorter time periods are associated with the flow passage across the wing chord outboard than the MAC. Therefore, accurately resolving the flow in the wingtip region likely calls for higher grid resolution than elsewhere, as well as enhanced temporal accuracy.

V. Conclusions

This paper presents the implementation and assessment of Wall-Modeled Large-Eddy Simulation (WMLES) methodology in an unstructured-grid, node-centered flow solver, FUN3D, based on both finite-volume (FV) and finite-element (FE) discretizations that provide formal second-order spatial accuracy. Large-Eddy Simulation (LES) techniques resolve large-scale turbulent-flow features while modeling small-scale effects using the Vreman subgrid-scale model. At solid wall boundaries, a shear-stress model is employed. Here, the tangential flow velocities are extracted at

predetermined exchange locations from the LES solution, after which the solution to the wall model is obtained using Newton iterations to ultimately obtain the wall shear stress, which is then used to provide a proper boundary-flux closure. The exchange location is utilized to communicate between the LES region and wall boundaries and is currently selected as the first point off the wall for both FV and FE discretization methods. The nonlinear equations representing conservation of spatially-filtered mass, momentum, and energy are integrated in time using either an optimized second-order accurate backward difference formula or a two-stage implicit Runge-Kutta temporal scheme.

Two high-lift configurations of interest have been used to assess the capabilities of the WMLES approaches, including the McDonnell Douglas 30P30N multielement airfoil and a NASA High-Lift Common Research Model (CRM-HL). In the 30P30N multielement airfoil example, the focus is placed on examining whether WMLES technology is successful in capturing changes in key aerodynamic characteristics and boundary-layer profiles caused by increasing Reynolds number at different angles of attack. Numerical results obtained based on FUN3D-FV WMLES show that correct trends in the variations of integrated aerodynamic forces and moments, surface pressure distributions, and boundary-layer/wake profiles at various chordwise stations are captured as the Reynolds number increases from 5 million to 9 million.

In the CRM-HL example, the emphasis centers on assessment of WMLES solutions and the model capabilities for maximum-lift ($C_{L,max}$) predictions in support of the certification by analysis endeavor. Free-air simulations conducted using both FUN3D-FV and FUN3D-FE solvers are included and compared with wall-corrected experimental data for a range of angles of attack. WMLES using the FUN3D-FV solver have been performed on three computational grids consisting of 555 million, 419 million, and 156 million points, namely Meshes A^+, A, and B, respectively. The FUN3D-FE solver has been used on Mesh B. Lift, drag, and pitching moment polars are accurately predicted by the two solvers for various flight regimes including the linear portion of the lift curve slope, maximum lift, and post-stall regimes. The computed lift coefficient corresponding to the experimental maximum lift agrees very well with the measurement within a small 1% deviation. At the highest angle of attack (21.47°) corresponding to the available experimental data, a pitch-break phenomenon present in the experiments is not replicated in the WMLES solutions produced by either solver. However, the FUN3D-FV WMLES computations at the angle of attack of 22.0° successfully capture the pitch break and show significantly improved agreement on the surface pressures near the wing-root regions as compared to the experiments. This discrepancy in the pitching moment predictions is possibly caused by the lack of wind-tunnel wall effects in the free-air simulations. Numerical studies of $C_{L,max}$ predictions for another CRM-HL configuration in the ecosystem that examines Reynolds number effects will be systematically conducted in future work through free-air and wind-tunnel modeling simulations.

Acknowledgments

This research is sponsored by the NASA Transformational Tools and Technologies (TTT) Project of the Transformative Aeronautics Concepts Program under the Aeronautics Research Mission Directorate (ARMD). The authors would like to acknowledge Aaron Walden, Gabriel Nastac, and Christopher Stone for their assistance with the implementation. The authors further acknowledge the Langley GEOmetry LABoratory (GEOLAB) for grid generation. Resources supporting this work are provided by the NASA High-End Computing (HEC) Program through the NASA Advanced Supercomputing (NAS) Division at Ames Research Center.

References

[1] Mauery, T., Alonso, J., Cary, A., Lee, V., Malecki, R., Mavriplis, D., Medic, G., Schaefer, J., and Slotnick, J., "A Guide for Aircraft Certification by Analysis," NASA CR-20210015404, NASA, May 2021.

[2] NASA and AIAA, "1st High-Lift Prediction Workshop," , June 26, 2010 [Online]. URL `https://hiliftpw.larc.nasa.gov/index-workshop1.html`.

[3] NASA and AIAA, "2nd High-Lift Prediction Workshop," , June 22–23, 2013 [Online]. URL `https://hiliftpw.larc.nasa.gov/index-workshop2.html`.

[4] NASA and AIAA, "3rd High-Lift Prediction Workshop," , June 3–4, 2017 [Online]. URL `https://hiliftpw.larc.nasa.gov/index-workshop3.html`.

[5] NASA and AIAA, "4th High-Lift Prediction Workshop," , November 21, 2021 [Online]. URL `https://hiliftpw.larc.nasa.gov/`.

[6] Wang, L., Anderson, W. K., Nielsen, E. J., Balakumar, P., Park, M. A., Carlson, J.-R., Iyer, P. S., and Diskin, B., "Wall-Modeled Large-Eddy Simulations for High-Lift Configurations using FUN3D," AIAA Paper 2022–1555, 2022.

[7] Anderson, W. K., Newman, J. C., and Karman, S. L., "Stabilized Finite Elements in FUN3D," *Journal of Aircraft*, Vol. 55, No. 2, 2018, pp. 696–714.

[8] Valarezo, W. O., Dominik, C. J., McGhee, R. J., and Goodman, W. L., "High Reynolds Number Configuration Development of A High-Lift Airfoil," AGARD Meeting in High-Lift Aerodynamics, CP 515, July 6–9 1992.

[9] Chin, V., Peters, D. W., Spaid, F. W., and McGhee, R. J., "Flowfield Measurements about A Multielement Airfoil at High Reynolds Numbers," AIAA Paper 93–3137, 1993.

[10] Klausmeyer, S. M., and Lin, J. C., "Comparative Results from a CFD Challenge Over a 2D Three-Element High-Lift Airfoil," NASA Technical Memoranda TM-112858, May 1997.

[11] Anderson, W. K., Bonhaus, D. L., McGhee, R. J., and Walker, B. S., "Navier-Stokes Computations and Experimental Comparisons for Multielement Airfoil Configurations," *Journal of Aircraft*, Vol. 32, No. 6, 1995, pp. 1246–1253.

[12] White, F. M., and Corfield, I., *Viscous Fluid Flow*, Vol. 3, McGraw-Hill New York, 2006.

[13] Vreman, A. W., "An Eddy-Viscosity Subgrid-Scale Model for Turbulent Shear Flow: Algebraic Theory and Applications," *Physics of Fluids.*, Vol. 16, No. 10, 2004, pp. 3670–3681.

[14] Anderson, W. K., and Bonhaus, D. L., "An Implicit Upwind Algorithm for Computing Turbulent Flows on Unstructured Grids," *Computers & Fluids*, Vol. 23, No. 1, 1994, pp. 1–21.

[15] Biedron, R. T., Carlson, J.-R., Derlaga, J. M., Gnoffo, P. A., Hammond, D. P., Jones, W. T., Kleb, B., Lee-Rausch, E. M., Nielsen, E. J., Park, M. A., Rumsey, C., Thomas, J. L., Thompson, K. B., Walden, A. C., Wang, L., and Wood, W. A., "FUN3D Manual: 13.7," NASA/TM-0205010139, 2019.

[16] Roe, P. L., "Approximate Riemann Solvers, Parameter Vectors, and Difference Schemes," *Journal of Computational Physics*, Vol. 43, No. 2, 1981, pp. 357–372.

[17] Burg, C., "Higher Order Variable Extrapolation for Unstructured Finite Volume RANS Flow Solvers," AIAA Paper 2005–4999, 2005.

[18] van Leer, B., "Towards the Ultimate Conservative Difference Scheme, V. A Second Order Sequel to Godunov's Method," *Journal of Computational Physics*, Vol. 32, No. 1, 1979, pp. 101–136.

[19] Thomas, J. L., Diskin, B., and Nishikawa, H., "A Critical Study of Agglomerated Multigrid Methods for Diffusion on Highly-Stretched Grids," *Computers & Fluids*, Vol. 41, No. 1, 2011, pp. 82–93.

[20] Diskin, B., and Thomas, J. L., "Accuracy Analysis for Mixed-Element Finite-Volume Discretization Schemes," NIA Technical Report 2007-8, 2007.

[21] Thomas, J. L., Diskin, B., and Rumsey, C., "Towards Verification of Unstructured Grid Methods," *AIAA Journal*, Vol. 46, No. 12, 2008, pp. 3070–3079.

[22] Kawai, S., and Larsson, J., "Wall-Modeling in Large Eddy Simulation: Length Scales, Grid Resolution, and Accuracy," *Physics of Fluids*, Vol. 24, No. 1, 2012, p. 015105.

[23] Spalding, D. B., "A Single Formula for the "Law of the Wall"," *J. Appl. Mech.*, Vol. 28, No. 3, 1961, pp. 455–458.

[24] Carlson, J.-R., Vatsa, V. N., and White, J., "Validation of A Node-Centered Wall Function Model for the Unstructured Flow Code FUN3D," AIAA Paper 2015–2758, 2015.

[25] Vatsa, V., Carpenter, M. H., and Lockard, D., "Re-evaluation of An Optimized Second Order Backward Difference (BDF2OPT) Scheme for Unsteady Flow Applications," AIAA Paper 2010–0122, January 4–7 2010.

[26] Wang, L., Diskin, B., Nielsen, E., and Liu, Y., "Improvements in Iterative Convergence of FUN3D Solutions," AIAA Paper 2021–0857, 2021.

[27] Anderson, W. K., and Newman, J. C., "High-Order Stabilized Finite Elements on Dynamic Meshes," AIAA Paper 2018–1307, 2018.

[28] Newman, J. C., and Anderson, W. K., "Investigation of Unstructured Higher-Order Methods for Unsteady Flow and Moving Domains," AIAA Paper 2015–2917, 2015.

[29] Saad, Y., and Schultz, M. H., "GMRES: A Generalized Minimum Residual Algorithm for Solving Nonsymmetric Linear Systems," *SIAM J. Scientific and Statistical Computing.*, Vol. 7, No. 3, 1986, pp. 856–869.

[30] Saad, Y., *Iterative Methods for Sparse Linear Systems*, 2nd ed., Society for Industrial and Applied Mathematics, Philadelphia, PA, USA, 2003.

[31] Wood, S., Jones, W., Jacobson, K., and Anderson, K., "Sparse Linear Algebra Toolkit for Computational Aerodynamics," AIAA Paper 2020–0317, 2020.

[32] Stainback, P. C., McGhee, R. J., Beasley, W. D., and Morgan, H. L., "The Langley Research Center's Low Turbulence Pressure Tunnel," AIAA Paper 1986–0762, 1986.

[33] Klausmeyer, S. M., and Lin, J. C., "Comparative Results from A CFD Challenge Over a 2D Three-Element High-Lift Airfoil," NASA /TM-112858, 1997.

[34] Bodart, J., and Larsson, J., "Wall-Modeled Large Eddy Simulation of the McDonnell-Douglas 30P/30N High-Lift Airfoil in Near-Stall Conditions," AIAA Paper 2012–3022, 2012.

[35] Bodart, J., Larsson, J., and Moin, P., "Large Eddy Simulation of High-Lift Devices," AIAA Paper 2013–2724, 2013.

[36] Angelino, M., Fernandez-Yanez, P., Xia, H., and Page, G., "Large-Eddy Simulation with Modeled Wall Stress for Complex Aerodynamics and Stall Prediction," *AIAA Journal*, Vol. 59, No. 4, 2021, pp. 1225–1237.

[37] Allmaras, S. R., Johnson, F. T., and Spalart, P. R., "Modifications and Clarifications for the Implementation of the Spalart-Allmaras Turbulence Model," Seventh International Conference on Computational Fluid Dynamics (ICCFD7), July 9–13 2012.

[38] Evans, A. N., Lacy, D. S., Smith, I., and Rivers, M. B., "Test Summary of the NASA High-Lift Common Research Model Half-Span at QinetiQ 5-Metre Pressurized Low-Speed Wind Tunnel," AIAA Paper 2020–2770, 2020.

[39] Ahmad, N. N., Wang, L., Anderson, W. K., Balakumar, P., Iyer, P. S., and Nielsen, E. J., "FUN3D Simulations for the 4th AIAA High-Lift Prediction Workshop," AIAA Paper 2022–3436, 2022.

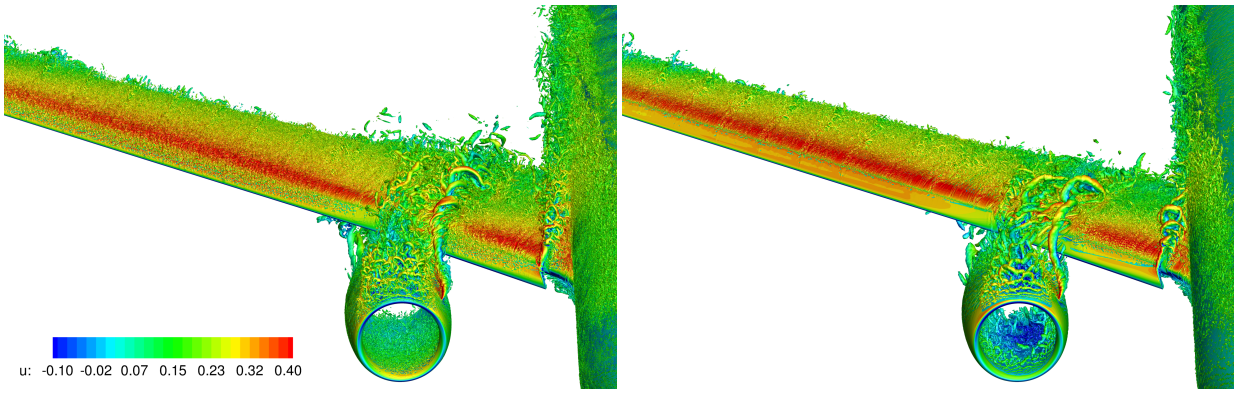

(a) Front view, FUN3D-FV

(b) Front view, FUN3D-FE

(c) Side view, FUN3D-FV

(d) Side view, FUN3D-FE

Fig. 24 Isosurfaces of q-criterion around CRM-HL configuration at $\alpha = 21.47°$ obtained by FUN3D-FV on Mesh A$^+$ and FUN3D-FE on Mesh B, colored by instantaneous streamwise velocity. Values of q-criterion are set to 0.002 and 0.00025.

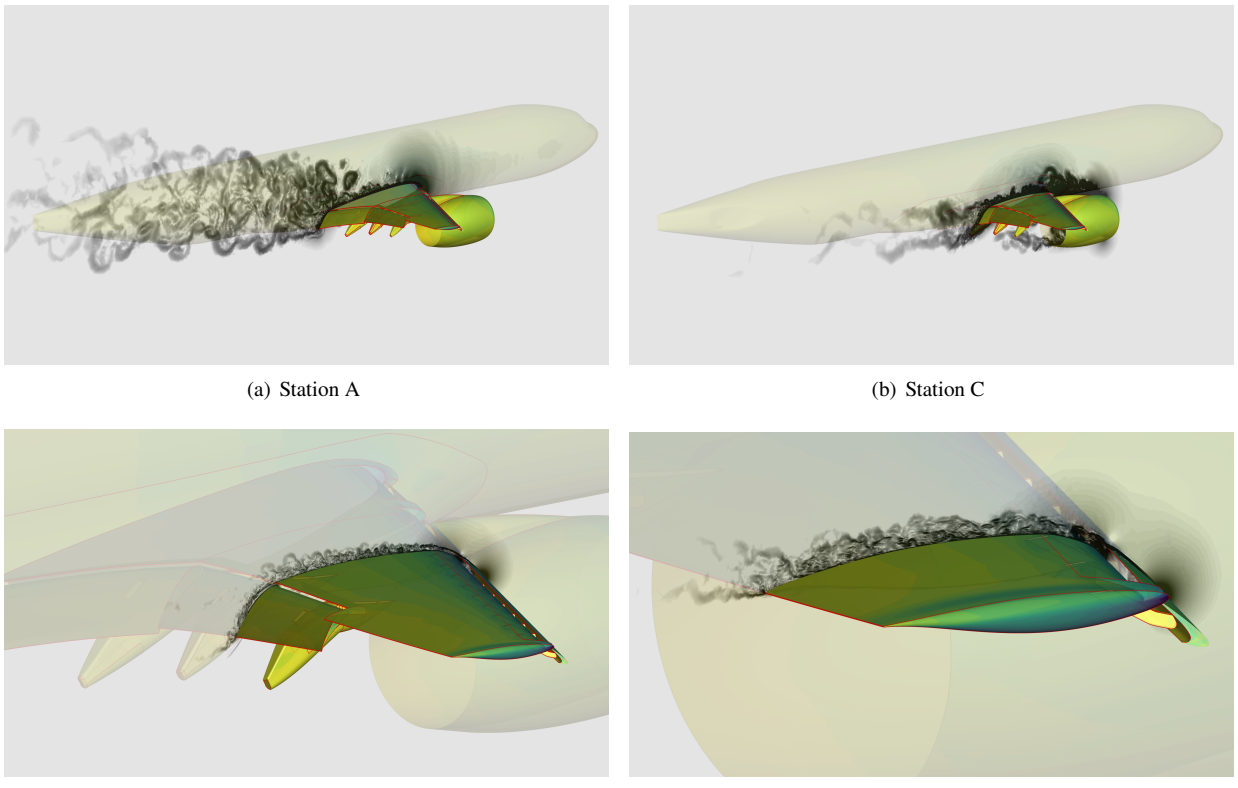

(a) Station A

(b) Station C

(c) Station E

(d) Station H

Fig. 25 Contours of density-gradient magnitude at different spanwise stations obtained by FUN3D-FE on Mesh B ($\alpha = 21.47°$); surface colored by time-averaged pressure).

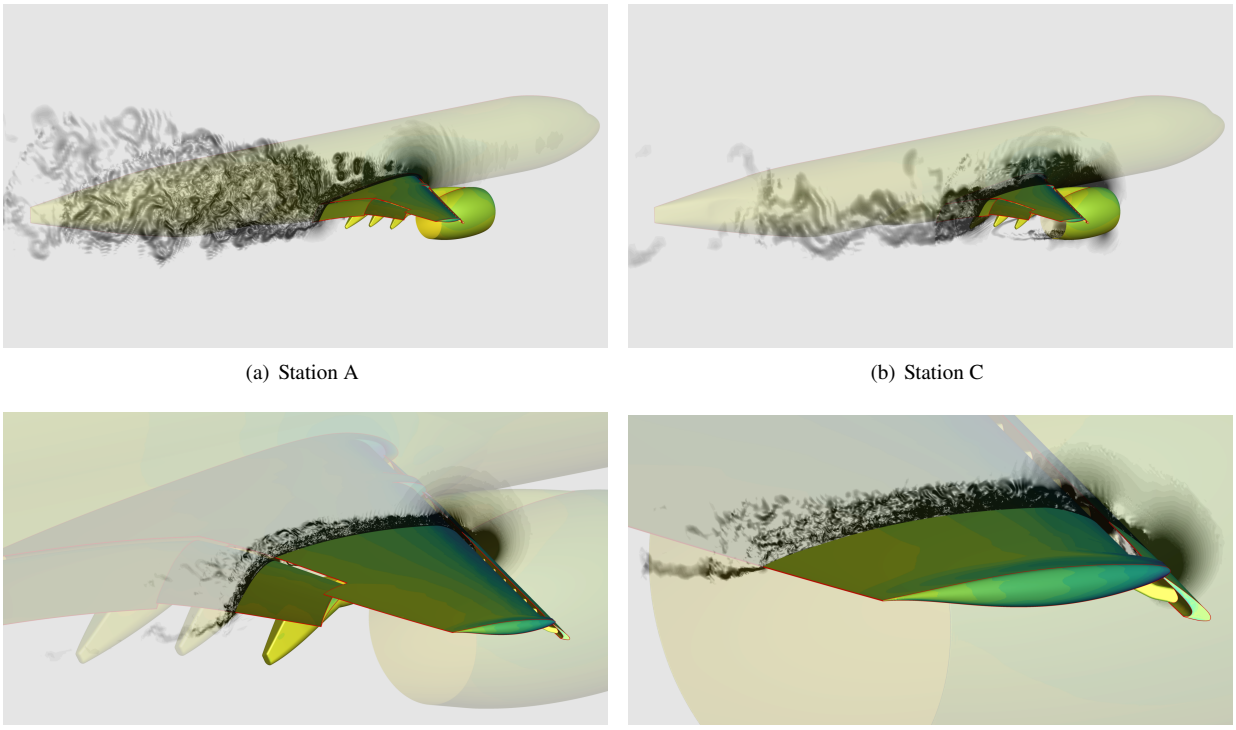

(a) Station A

(b) Station C

(c) Station E

(d) Station H

Fig. 26 Contours of density-gradient magnitude at different spanwise stations obtained by FUN3D-FV on Mesh A$^+$ ($\alpha = 21.47°$); surface colored by time-averaged pressure).

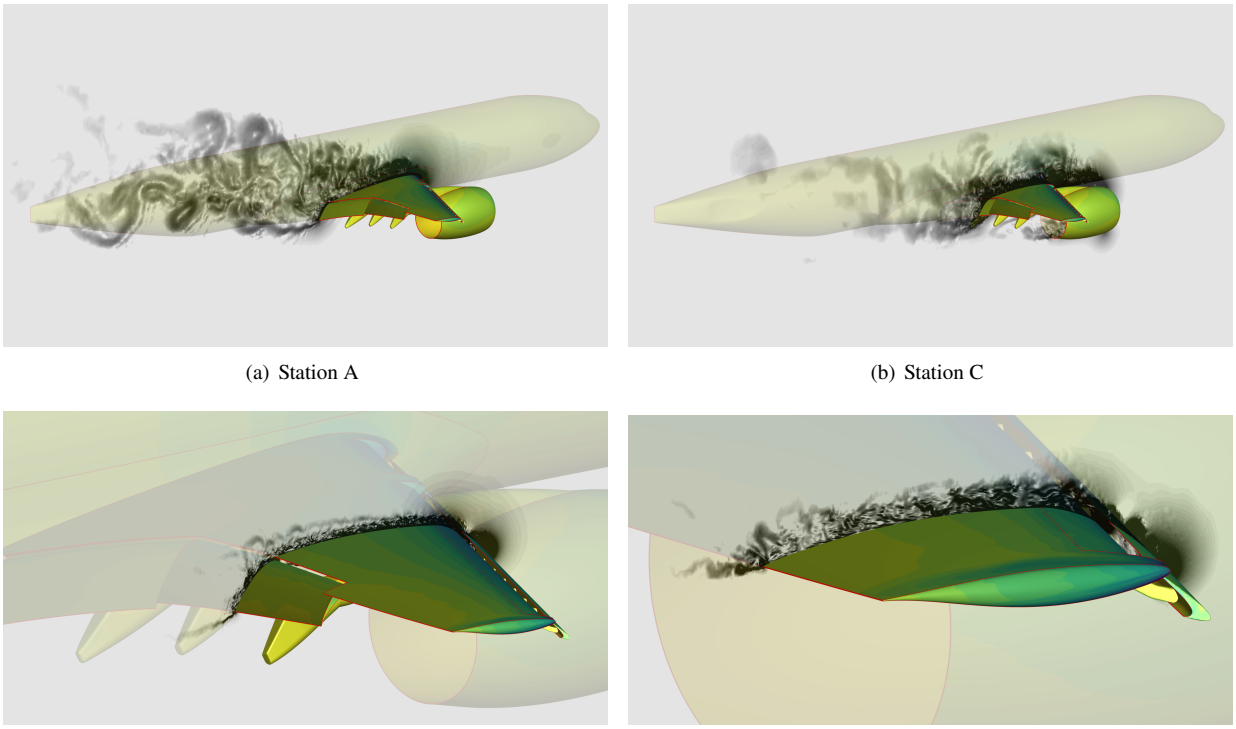

(a) Station A

(b) Station C

(c) Station E

(d) Station H

Fig. 27 Contours of density-gradient magnitude at different spanwise stations obtained by FUN3D-FV on Mesh B ($\alpha = 21.47°$); surface colored by time-averaged pressure).